DIPLOMARBEIT

TRANSITION OF TU WIEN CHANGE DETECTION METHOD FROM ASAR TO SENTINEL-1: A STATISTICAL ANALYSIS.

Ausgeführt am Institut für Photogrammetrie und Fernerkundung
zum Zwecke der Erlangung des akademischen Grades eines Diplom-Ingenieur

unter der Leitung von
Univ.Prof. Dipl.-Ing. Dr.techn. Wolfgang Wagner

und der Betreuung durch
Dipl.-Ing. Bernhard Bauer-Marschallinger

eingereicht an der Technischen Universität Wien
Fakultät für Mathematik und Geoinformation
von

SIMON HOCHSTÖGER

Matrikelnummer 1027106
Aegidigasse 24/10-11
1060 Wien

Wien, am 27. Juni 2016   . . . .

Abstract

Soil moisture is an important variable in the hydrological and meteorological cycle of the earth. It can have profound impacts on the planet's climate system and also influences processes such as flooding and runoff generation or drought developments. Hence, the knowledge of the distribution and amount of water in the soil is of great interest for many applications.

The Remote Sensing Research Group at TU Wien developed a method to retrieve soil moisture from backscatter measurements obtained from active microwave sensors. This method was initially developed for scatterometer data, but was then also adapted for the Advanced Synthetic Aperture Radar (ASAR) on board of the Envisat satellite. In 2014, the first of two Sentinel-1 satellites was launched into its orbit, carrying a synthetic aperture radar (SAR) that is similar to the ASAR instrument. Consequently, a transfer of the ASAR soil moisture algorithm to Sentinel-1 was expected to be straight forward.

The aim of this thesis is to investigate if the ASAR soil moisture algorithm can be transferred to Sentinel-1 using retrieval parameters calculated from ASAR Wide Swath (WS) data. Due to the lack of historical data, it is not yet feasible to derive the model parameters that are needed in the retrieval from Sentinel-1 data itself. Therefore the Sentinel-1 surface soil moisture (SSM) was calculated with ASAR WS parameters and compared to the ASAR SSM products using coarse spatial resolution soil moisture acquisitions from the Advanced Scatterometer (ASCAT) and from the Global Land and Data Assimilation System (GLDAS). The evaluation of the different products was performed over central Europe by calculation standard performance metrics, i.e. the temporal correlation and the root mean square difference (RMSD) of the SSM time series. Furthermore, the correlation and the RMSD were determined for different land cover types.

The results show a better correlation and RMSD performance for ASAR WS than for Sentinel-1, which can be explained with the smaller sample size and shorter period of Sentinel-1 dataset. Furthermore, if one wants to realise the full potential of Sentinel-1 for soil moisture retrieval, then (i) an adaptation of the model and (ii) the calibration of the model parameters with Sentinel-1 data should be considered.

Kurzfassung

Bodenfeuchte übernimmt eine wichtige Rolle im hydrologischen und meterologischen Zyklus der Erde. Sie kann tiefgreifende Auswirkungen auf das Klimasystem des Planeten haben und beeiflusst auch Prozesse wie Hochwasser und Dürre oder auch den Wasserabfluss. Daher ist die Kenntnis über die Verteilung und der Menge an Wasser im Boden von großem Interesse für viele Anwendungen.

Die Forschungsgruppe für Fernerkundung an der TU Wien hat eine Methode entwickelt, die Bodenfeuchteinformationen aus Rückstreuungsmessungen von aktiven Mikrowellensensoren gewinnt. Dieses Verfahren wurde zuerst für Scatterometerdaten entwickelt, danach aber auch für das *Advanced Synthetic Aperture Radar* (ASAR) an Bord des Satelliten Envisat angepasst. 2014 wurde der erste von zwei Sentinel-1 Satelliten in seine Umlaufbahn gebracht, der ein *Synthetic Aperture Radar* an Bord hat, das sehr ähnlich dem ASAR instrument ist. Folglich wurde ein Transfer des ASAR Bodenfeuchte-Algorithmus zu Sentinel-1 für möglich gehalten.

Das Ziel dieser Arbeit ist zu untersuchen, ob der für ASAR angepasste Bodenfeuchte-Algorithmus mit Hilfe der ASAR Wide Swath (WS) Modellparameter auf Sentinel-1 übertragen werden kann. Aufgrund fehlender historischer Daten ist es noch nicht möglich die im Algorithmus gebrauchten Parameter nur von Sentinel-1 Daten zu berechnen. Daher wurde die Sentinel-1 Oberflächenbodenfeuchte mit ASAR WS Parametern berechnet und mit Hilfe von räumlich grob augelösten Daten von *Advanced Scatterometer* (ASCAT) und *Global Land and Data Assimilation System* (GLDAS) mit der ASAR Bodenfeuchte verglichen. Der Vergleich der verschiedenen Produkte wurde über einem Gebiet in Mitteleuropa durchgefüht. Zur Berechnung herangezogen wurden die zeitliche Korrelation, sowie die mittlere quadratische Abweichung der Bodenfeuchtezeitserien. Des Weiteren sind die Korrelationen und mittleren quadratischen Abweichungen auch speziell für verschiedene Bodenbedeckungsarten bestimmt worden.

Die wichtigsten Ergebnisse zeigen bessere Korrelations- und RMSD Werte für ASAR WS als für Sentinel-1. Dies kann mit der geringeren Anzahl an Daten, sowie mit dem kürzeren Zeitraum der Sentinel-1 Daten erklärt werden. Falls man das gesamte Potential von Sentinel-1 für die

Bodenfeuchtebestimmung ausnützen möchte, sollte (i) eine Anpassung des Modells und (ii) die Kalibrierung der Modellparameter mit Sentinel-1 Daten berücksichtigt werden.

Danksagung

Diese Diplomarbeit entstand am Department für Geodäsie und Geoinformation der TU Wien. Ich möchte mich daher bei allen Kollegen bedanken, die immer ein offenes Ohr für meine Fragen hatten und mir mit vielen Ratschlägen weiterhelfen konnten. An dieser Stelle möchte ich mich besonders bei meinen Betreuern Wolfgang Wagner und Bernhard Bauer-Marschallinger bedanken, die mich jederzeit mit ihrer Fachkenntnis unterstützt haben. Besonders die vielen Diskussionen mit Bernhard haben mich immer wieder vorangetrieben und schlussendlich geholfen diese Arbeit fertigzustellen.

Ich möchte mich auch bei allen meinen Freunden und Studienkollegen bedanken, die mich nicht nur während des Schreibens der Diplomarbeit, sondern während des gesamten Studiums begleitet und unterstützt haben und mich auch mal vom Studium abgelenkt haben. Besonderer Dank gilt auch meiner Freundin, ohne ihre Geduld und Unterstützung wären die letzten Monate sicher nicht so gut verlaufen. Den größten Dank möchte ich aber meinen Eltern und meiner gesamten Familie aussprechen, die dieses Studium erst ermöglicht haben.

Contents

List of Acronyms

ASAR	Advanced Synthetic Aperture Radar
ASCAT	Advanced Scatterometer
CL	Correlation Layer
CLC	Corine Land Cover
CMASK	Correlation Mask
CORINE	Coordination of Information on the Environment
EC	European Commission
ERS	European Remote Sensing Satellite
ESA	European Space Agency
GLDAS	Global Land Data Assimilation System
GM	Global Monitoring Mode
IW	Interferometric Wide Swath Mode
METOP	Meteorological Operational Platform
RMSD	Root Mean Square Difference
SAR	Synthetic Aperture Radar
SMSA	Soil Moisture Sensitive Areas
SNR	Signal-to-Noise Ratio
SSM	Surface Soil Moisture
WGS	World Geodetic System
WS	Wide Swath Mode

List of Figures

List of Tables

Chapter 1

Introduction

Water is the Earth's most important resource for the life of humans, flora and fauna and the circulation and distribution of water has an essential impact on our climate system. *Soil moisture* is only a percentage of 0.001% - 0.005% of this total amount of water, but it plays a very important role in the environment and our climate system. In general, soil moisture is defined as the water contained in the unsaturated soil zone (see Figure 1.1). While roughly one half of the soil's volume is composted of mineral and organic content, the other half consists of pores. Soil moisture refers to the amount of water contained in these pores [Hillel, 1998].
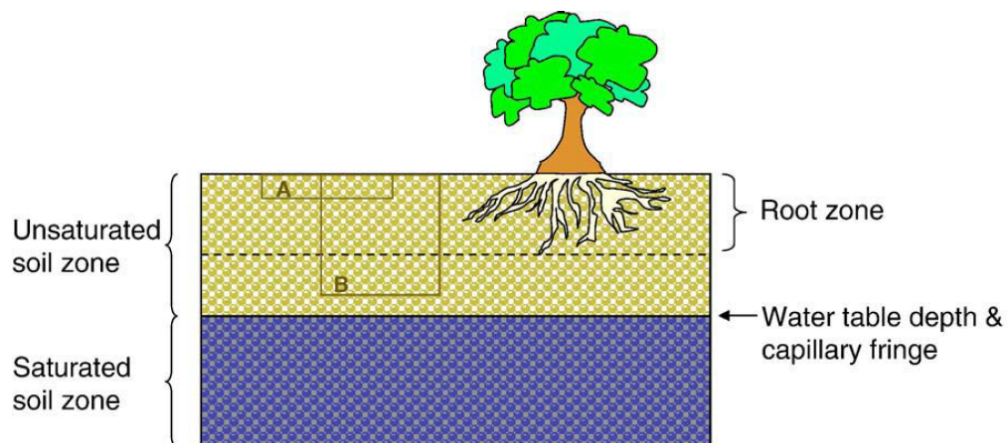

Figure *1.1: The saturated and unsaturated soil zones [Seneviratne et al., 2010].*

There are various reasons why the knowledge of the soil moisture content is of great interest. Soil moisture controls the partitioning between infiltration and runoff. For instance, during precipitation events, the infiltration rate is controlled by soil moisture, which consequently determines

the amount of runoff produced. Also the degree of prior saturation is an important control on river catchment response to rainfall or snowmelt and subsequent flood generation. Overland flow will be larger and will occur more quickly on wetter soils and in catchments, where the soil is more saturated [Petropoulos et al., 2013].

As an essential water source for vegetation, soil moisture determines the growth and healthiness of the plants, because in contrast to precipitation, which is only available at short notice, soil moisture serves as a longer preserved water reservoir for plants. All in all, soil moisture is a key parameter in the global water, energy and carbon cycles and plays an important role in hydrology, meteorology, climatology and agronomy.

The large spatial and temporal heterogeneity of soil moisture makes it a difficult parameter to measure on a routine basis over large areas. However, there are several measurement techniques for retrieving information about the soil moisture content (see Chapter 2). Some of these techniques are able to measure soil moisture very accurate and with a high temporal resolution but they are only representative for a small area. That is, these techniques are not able to capture soil moisture on a large scale. On the other hand, satellite remote sensing has the capability to monitor soil moisture conditions over large areas and at regular time intervals.

Most remote sensing satellites circle the Earth in a polar orbit with altitudes ranging from 300 km to 800 km. At these altitudes, the satellites must orbit at a very high speed, which allows them to complete one orbit in about 90 minutes. Consequently they are able to cover almost the entire Earth in a short period of time. In 1991 the European Space Agency (ESA) started its first Earth-observing satellite program. The European Remote Sensing (ERS) satellites, ERS-1 and ERS-2, were launched into the same polar orbit in 1991 and 1995, respectively. Among others, each satellite carried a scatterometer, which scans the Earth's surface by transmitting a pulse of microwave energy and measuring the backscattered signal. It is this backscattered signal, which is, among others, dependent on the water content of the soil.

Wagner et al. (1999) developed a soil moisture retrieval algorithm for the ERS scatterometer. This algorithm, which will in the following be referred to as the TU-Wien model, estimates the soil moisture by relating the backscatter value to dry and wet soil conditions. Dry and wet conditions refer to a completely dry soil and a saturated soil, respectively. The references for dry and wet soil conditions, as well as a parameter accounting for vegetation effects, are the main parameters in the TU-Wien model. These parameters can solely be derived from historical data from the instrument itself. Based on the existing algorithm, Naeimi et al. (2009) presented an improved TU-Wien model for ERS and MetOp scatterometers. Those sensors deliver surface soil moisture (SSM) with a spatial resolution of about 25-50 km, which is sufficient for many

applications, e.g. numerical weather predictions or climate research. But there is also a need for observations at finer scale, e.g. for hydrological applications or agricultural monitoring and irrigation management [Loew et al., 2006].

High-resolution soil moisture can be obtained from Synthetic Aperture Radar (SAR) instruments. Hence, Pathe et al. (2009) used an adapted version of the soil moisture retrieval algorithm to retrieve soil moisture from Envisat Advanced Synthetic Aperture Radar (ASAR) measurements. Due to the acquisition strategy of ASAR, only an irregular and much reduced coverage of the earth's surface was reached, which is not beneficial for the above applications.

In April 2014, the first of two Sentinel-1 satellites, Sentinel-1A, was launched into space. Sentinel-1 is the first mission that provides high-resolution SAR data on an operational basis using a fixed acquisition strategy [Torres et al., 2012]. The Sentinel-1 sensor is an active microwave system operating at a central frequency (5.405 GHz) that is very close to that of ASAR (5.331 GHz). Therefore, the transfer of the SSM retrieval algorithm to Sentinel-1 has been foreseen in several studies [Wagner et al. (2009); Gruber et al. (2013); Hornacek et al. (2012)].

The Remote Sensing Research Group at the TU Wien already realised the transfer of the Envisat SSM algorithm to Sentinel-1. Due to lack of historical data for Sentinel-1 (data is only available for the short period of October 2014 to January 2016) it is not yet possible to derive the model parameters of the retrieval algorithm from Sentinel-1 data itself. However, because of the similar sensor design of Envisat ASAR and Sentinel-1, the parameters derived from ASAR Wide Swath data are used for the soil moisture retrieval with Sentinel-1.

The objective of this work is to investigate if and how the transfer of the Envisat algorithm to Sentinel-1 and also the usage of the Envisat model parameters affects the retrieved Sentinel-1 soil moisture data. The differences in the observing frequency and observing geometry, the highly improved radiometric resolution for Sentinel-1, the different temporal resolutions or a possible different sensor calibration may influence the Sentinel-1 retrieval algorithm performance.

The structure of the work is as follows: The second chapter will give an overview of the theoretical basis of remote sensing of soil moisture, also the soil moisture retrieval algorithm for Envisat ASAR and Sentinel-1 is explained in greater detail, including the already mentioned parameters.
Chapter 3 describes the properties of Envisat ASAR and Sentinel-1 and their soil moisture datasets, also the reference datasets for the evaluation are introduced here.
Chapter 4 introduces the different methods that are used to perform the validation of the Sentinel-1 and ASAR SSM data. A correlation analysis, as well as a root mean squared

difference analysis, including the analysis of different land cover types, are the main subject of this chapter.

Then, Chapter 5 describes the results of the in chapter 4 introduced methods and also visually compares the different datasets. At the end of this chapter, the results are discussed.

Chapter 6 provides a summary of the study, the obtained results and looks into possible future developments.

Chapter 2

Soil moisture and Remote Sensing

Soil moisture is generally defined as the water contained in the unsaturated soil surface of the Earth, fed by rainfall, snowmelt, or capillary attraction from groundwater. Soil moisture is affected by the soil texture, topography, land cover and climate, and as a result, it is highly variable both in space and time [Petropoulos et al., 2013]. Besides, soil moisture can also be separated into surface soil moisture (defined as the water contained within the first 5 cm of the soil depth) and root zone soil moisture (defined as the water content below 5 cm of soil depth, [Seneviratne et al., 2010], see Figure 1.1). One measure commonly used to define the water content in the soil volume V is the *volumetric soil moisture θ* (e.g. volumes A or B in Figure 1.1), which is defined as follows:

$$\theta = \frac{volume\ of\ water\ in\ V}{V} \qquad [m^3_{H_2O}/m^3_{soil}] \qquad (2.1)$$

Measurement Techniques There are several different ways to measure the water content in the soil: (1) In laboratory, for example the thermogravimetric method requires oven dying of a known volume of soil and determining the weight loss. This method is very precise, but bears the disadvantage that it is destructive to the sample (cannot be used for more than one measurement) and the samples must be obtained manually [Walker et al., 2004]. (2) In situ, soil moisture can be measured using measurement techniques, which measure for instance the dielectric properties of the soil, which are highly depended on the water content. (3) Another method is remote sensing of the surface with a microwave sensor on board of Earth observation satellites or airplanes. In the above order, these three methods have a decreasing measurement accuracy, but an increasing spatial coverage. While the soil sample only represents one certain spot of the surface and the in-situ measurements also the small surrounding area, remote sensing

offers an alternative to measure soil moisture at a variety of scales. Another difference of these three methods is the temporal resolution. In this regard the in-situ measurements are more or less constantly providing data, whereas satellite sensors are depended on the orbit configuration [Bauer-Marschallinger et al., 2015].

2.1 Microwave Remote Sensing

The microwave region of the electromagnetic spectrum extends over the frequency range of 0.3 to 300 GHz (or 1 m to 1 mm in wavelength). There are several reasons for using microwaves for remote sensing: microwave sensors provide their own illumination, they can be used day and night, without the necessity of the sun as a source of illumination. Another advantage is that microwaves can not only penetrate the atmosphere (Figure 2.1), but especially at longer wavelengths they are also able to penetrate clouds and rain, which makes them suitable to observe regions of the Earth, which are covered by clouds. They are also, to some extend, able to penetrate deeply into vegetation and also into the ground beneath. The interactions of
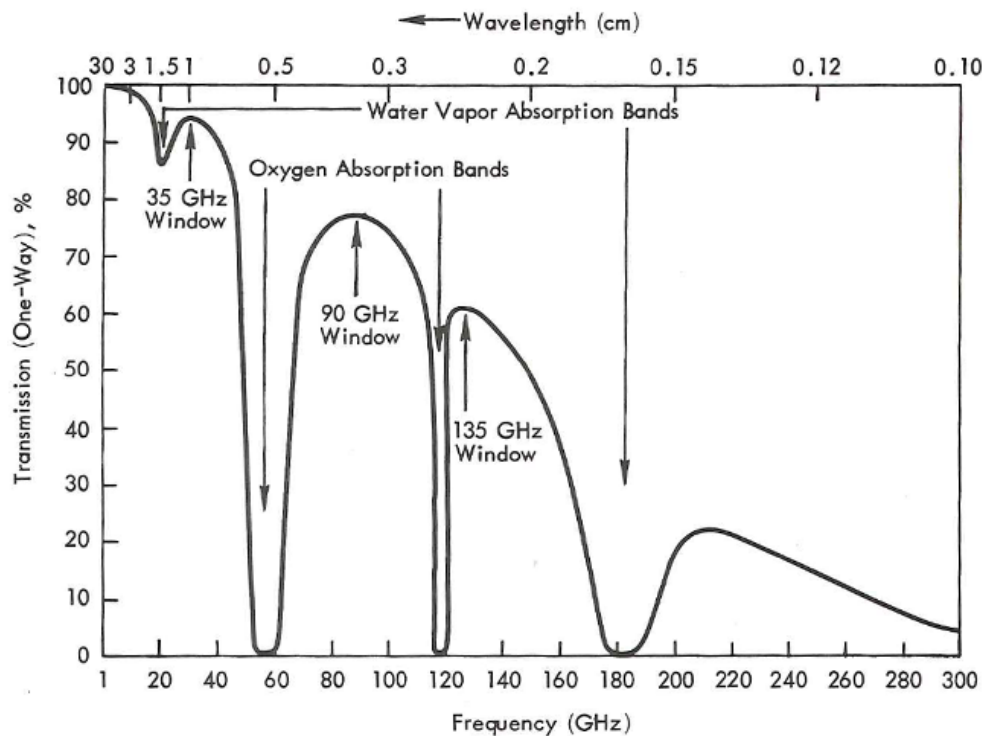
Figure 2.1: *Transmission of microwaves through the earth's atmosphere under clear sky conditions [Ulaby et al., 1981]*

microwaves with media are governed by different physical parameters, which makes them a useful tool for retrieving physical properties of the soil as for example soil moisture [Ulaby et al., 2014]. The theory behind using microwaves for remote sensing of soil moisture is based on the large contrast between the dielectric properties of liquid water and dry soil in the microwave region, which results in a high dependency of the soil on volumetric soil moisture [Barrett and Petropoulos, 2013]. In short, microwaves show a high sensitivity to the water content in the soil surface layer and are therefore highly suited for measuring soil moisture. Greater detail of the soil dielectric properties is given in section 2.1.3.

2.1.1 Radar Equation

The monostatic *radar equation* describes the process of a radar antenna emitting an electromagnetic wave which is scattered back from the earth's surface and detected at the same antenna again [Woodhouse, 2005]. The received power P_r of the backscattered signal can be written as:

$$P_r = \frac{P_t G_t A_r}{(4\pi)^2 R^4}\sigma \tag{2.2}$$

P_t is the emitted power from the radar antenna, G_t is the gain of the antenna, which describes the power that is emitted into target direction, $\frac{1}{(4\pi)^3 R^4}$ is the two-way spreading loss with the slant range R, A_r is the effective receiving area of the antenna and σ^0 is the radar cross section of the illuminated target. The radar cross section is a measure for the interaction of the incidence wave with the target and is highly dependent on the target's geometry and dielectric properties [Ulaby et al., 2014]. In general, an antenna footprint is usually a combination of many single targets with different shapes, which each contribute to σ. Therefore, the *backscattering coefficient* is defined in order to get a quantity that is independent of the areal extent of the target. The backscattering coefficient is the radar cross section normalized with the area:

$$\sigma^0 = \frac{d\sigma}{dA} \tag{2.3}$$

The dimensions of σ^0 is $m^2 m^{-2}$, but normally it is expressed on a logarithmic scale in decibels:

$$\sigma^0_{dB} = 10\,log\,\sigma^0 \tag{2.4}$$

The radar equation for an extensive area then yields to:

$$P_r = \int_A \frac{P_t G_t^2 \lambda^2}{(4\pi)^3 R^4} \sigma^0 dA \tag{2.5}$$

The received power P_r is normally converted to the backscattering coefficient in order to obtain information about the target.

2.1.2 Microwave Scattering Mechanisms

When a radar wave impinges on a surface at a specific incidence angle, a portion of the incidence wave is transmitted into the lower surface layer and another one is scattered back. The scattering component can be split into a portion which is scattered into all directions, this is referred to as diffuse scattering, and the rest is reflected in specular direction. Some of the diffuse scattering component returns to the sensor as backscatter [Ulaby et al., 2014]. There are two different scattering mechanisms.

Surface scattering   appears at a sharp boundary between two media, with different dielectric properties (e.g. air and soil). If an electromagnetic wave impinges on a smooth surface, one part of the wave is reflected back into the upper medium and the other part is transmitted into the lower medium. If a surface is rough (compared to the wavelength), also a diffuse scattering term is present. As the roughness of the surface increases, the specular refraction component decreases and the diffuse scattering component increases, which also increases the amount of backscatter, that returns to the sensor.

Volume scattering   occurs within the medium itself, in the case of an inhomogeneous medium. Small particles such as leaves, twigs or in general vegetation canopies can be such inhomogeneities, which diffusely scatter the wave back or attenuate or absorb the incoming wave. The surface scattering and volume scattering phenomena are illustrated in Figure 2.2.

Wet soils, for instance, act predominantly like a rough surface, which results in an increased backscatter coefficient, whereas very dry soils will act as volume scatters with microwaves scattered within the upper layers of the soil, which results in an attenuation of the signal [Woodhouse, 2005].
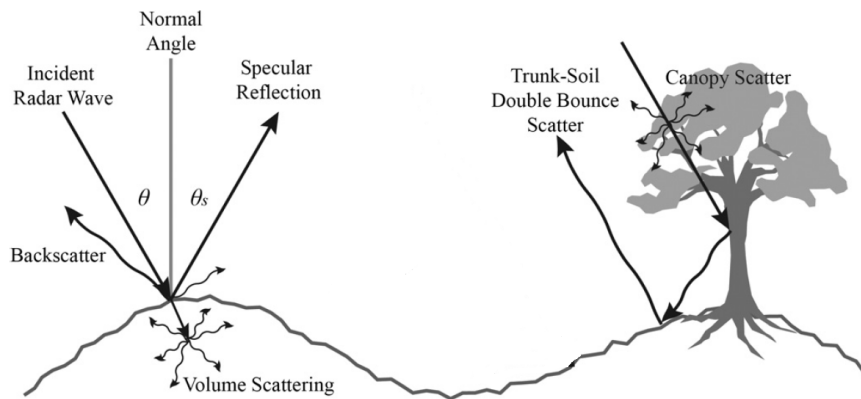
Figure 2.2: *Conceptual scattering of an incident radar signal by a rough and vegetated surface [Kornelsen and Coulibaly, 2013].*

Vegetation Effects Over vegetated surfaces the total acquired backscatter σ^0 consists of three scattering mechanisms:

- *Volume scattering*: direct backscatter of the incoming wave by vegetation canopy

- *Surface scattering*: scattering from the soil surface attenuated from the overlying vegetation

- *Surface-Volume interaction*: incoming wave, which is scattered downwards by the vegetation canopy and then scattered back from the soil surface, or vice versa

Compared to the surface and volume scattering term, the interaction term is usually assumed to be much smaller providing no significant contribution to the total backscatter value. As already mentioned above, bare soil scattering, with exception of very rough surfaces, is strongly dependent on the incidence angle. An increasing incidence angle results in a decreasing backscatter value. In contrast, the scattering from fully grown vegetation is quite uniform across a large incidence angle range. At smaller incidence angles, most of the radiation can penetrate through the vegetation so that the total backscatter is dominated by the surface scattering term. However, with an increasing incidence angle the incoming signal has a longer travel path through the canopy, so it gets more attenuated and the total reflected wave is dominated by the vegetation scattering term. In other words, at small incidence angles the overall backscatter from vegetated surfaces tends to be dominated by the surface scattering term, whereas at larger incidence angles volume scattering is the dominating term.

2.1.3 Soil Dielectric Properties

Microwave remote sensing is strongly influenced by the dielectric properties of soil. Amongst all natural media, water has the highest dielectric constant and as water is added to the soil, its dielectric constant increases. Due to its structure, water has a dipole character and in the presence of an electromagnetic field, the water molecules adjust their orientation to the electric field vector direction, which results in a high dielectric constant. The dielectric constant is also frequency depended. Especially the lower frequency domain from 1 to 10 GHz is dominated by high dielectric constants. Microwave sensors operate exactly in this region of the spectrum and therefore hold the largest potential for the retrieval of soil moisture [Pathe et al., 2009].

2.1.4 Active Microwave Sensors

Compared to passive sensors, which measure the microwave energy that is radiated (by thermal emission) or reflected (e.g. from the sun) by the earth's surface or atmosphere, active sensors generate their own illumination by transmitting microwave pulses and then measure the scattered signal. Spaceborne radar (radio detection and ranging) systems are generally classified in three categories: *Altimeter, Scatterometer* and *Synthetic Aperture Radar (SAR)*. Altimeters focus on measuring the time delay of the returned signal which provides distance information, whereas scatterometer and SAR are designed to accurately measure the properties of the echo (such as radar cross-sections, [Woodhouse, 2005]).

Scatterometer and SAR are side-looking radars, i.e. their antennas point to the side with a beam that is wide vertically and narrow horizontally. The spatial resolution of a side-looking radar is defined in two perpendicular dimensions: *range direction* is the direction perpendicular to the satellite flight track and *azimuth direction* is parallel to the orbit (Figure 2.3). The resolution in range direction is dependent on the length of the radar pulse - the shorter the pulse, the higher the resolution. One has to keep in mind that a shorter pulse length decreases the signal-to-noise ratio, which results in a lower radiometric resolution. Therefore most radar use combined pulse and frequency modulation techniques to obtain a higher resolution in range direction without a decreasing signal-to-noise ration. For real-aperture radar the spatial resolution in azimuth direction is dependent on the wavelength of the signal λ, the size of the antenna l and the height above the ground h:

$$r_a = \frac{\lambda h}{l \cos(\theta)} \qquad (2.6)$$
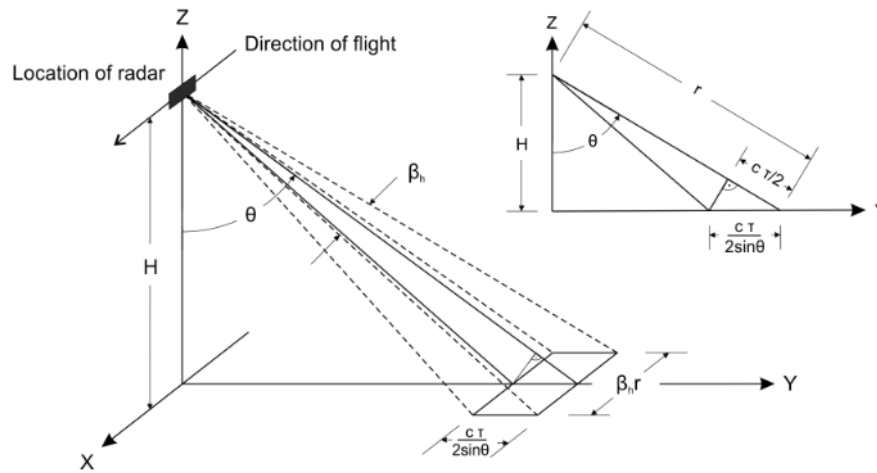
Figure 2.3: *Geometry of a side-looking aperture radar (after Ulaby et al. (1982)).*

Hence, to get a higher spatial resolution in azimuth direction when using the same frequency, a larger antenna is needed. In the spaceborne microwave domain this is an important limiting factor for the resolution of the sensor.

2.1.4.1 Scatterometers

Scatterometers are designed to measure the normalized radar cross section σ^0 (see Section 2.1.1) with high radiometric accuracy. To achieve such a high radiometric accuracy it is necessary to average the received pulses over a wide area, since single return pulses are typically noisy. This results in a relatively coarse spatial resolution of 25 - 50 km, but it does have the advantage of covering larger areas of the earth on a more frequent basis. Figure 2.4 shows for example the configuration of the antenna footprint of the Advanced Scatterometer (ASCAT) on board of a series of METOP satellites. This scatterometer uses a fan-beam antenna technology, where two sets of three antennas are arranged on each side broadside and +- 45° of broadside with respect to the satellite flight direction. With incidence angles ranging from 25° to 65°, ASCAT covers two 550km wide swaths to the left and right of the satellite ground. Considering this configuration, the daily global coverage of ASCAT is about 82% [Wagner et al., 2013].
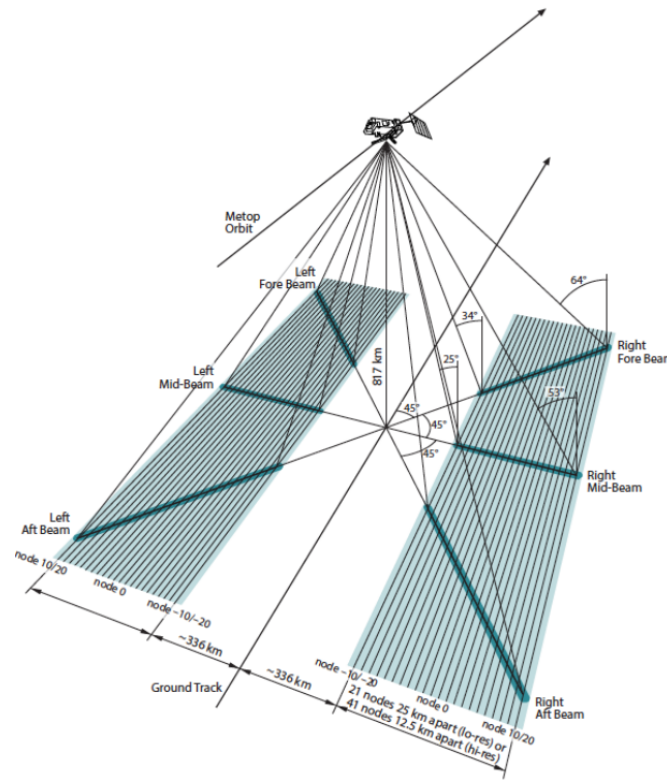
Figure 2.4: *Geometry of the Advanced Scatterometer (ASCAT) on board Metop satellites [Bartalis, 2009].*

2.1.4.2 Synthetic Aperture Radar

SAR sensors overcome the limitations to the resolution in azimuth direction by simulating one large antenna by the movement of one small antenna. The synthetic aperture technique is based on the fact that a target stays in the beam for a significant amount of time and is observed by the radar from different locations along track direction (Figure 2.5). As the SAR sensor is continuously moving, the return signal from the target will change in frequency as it passes through the radar beam, so that Doppler-shift processing can be used to locate from which part of the beam the echo returns from [Woodhouse, 2005]. The echoes returning from the front part of the beam are Doppler shifted to higher frequencies, while echoes from the aft part of the beam are Doppler shifted to lower frequencies. The change in frequency is given by:

$$f_D = \frac{V_{rel}}{\lambda} \quad [s^{-1}] \tag{2.7}$$

where V_{rel} is the relative motion between the transmitter and receiver and λ is the wavelength of the signal. Note that the antenna beam is now designed to be very wide in order to make the
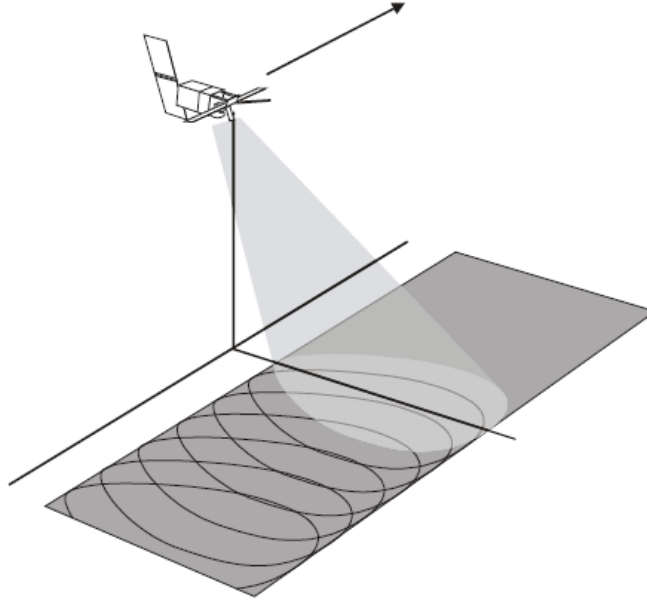
Figure 2.5: *Geometry of a SAR system [Woodhouse, 2005]. The beam is designed to be very wide, in order to have many overlapping footprints.*

footprints overlap. An increasing footprint size is caused by an decreasing antenna size and this also causes a wider range of available Doppler frequencies (Doppler bandwidth). The azimuthal spatial resolution of a SAR system is determined by the Doppler bandwidth as in:

$$r_a = \frac{V_s}{B_D} = \frac{V_s \lambda 2D}{4V_s \lambda} = \frac{D}{2} \tag{2.8}$$

where V_s is the relative velocity, D is the length of the real antenna and B_D is the Doppler bandwidth. This result implies that the azimuthal resolution is equal to half of the length of the antenna, so in contrast to real-aperture radar (equation 2.6) the resolution improves with decreasing antenna length. It is independent of the the distance of the sensor to the target and also independent of the wavelength of the signal. However, the high spatial resolution of SAR systems usually comes at the expense of a low-temporal resolution, because the these systems are typically limited by the power supply.

In short, scatterometers measure the radar cross section with a high radiometric accuracy by

averaging the returned signals, but this results in a low spatial resolution. In contrast, SAR achieves a very high spatial resolution in order of meters to hundreds of meters, but this comes at the expense of temporal and radiometric resolution as well as geographic coverage when compared to scatterometers.

2.2 Soil Moisture Retrieval Algorithm

Wagner et al. (1999) used the unique sensor design of the ERS scatterometer to develop a change detection method for retrieving soil moisture from radar measurements, the TU-Wien method. Later Naeimi et al. (2009) presented an improved soil moisture retrieval algorithm for ERS and MetOp scatterometers, based on the existing TU-Wien method, but with new parametrization as well as a series of modifications. Pathe et al. (2009) investigated if the SAR system onboard of Envisat can be used for retrieving soil moisture using a change detection approach, therefore the developed and later improved TU-Wien method was adapted for ASAR GM.

The TU-Wien method is a physically motivated empirical change detection method, that relates backscatter measurements $\sigma^0(\theta, t)$ to the highest and lowest values of $\sigma^0(\theta)$ that have ever been recorded. The highest and lowest values are references for the wettest and driest condition of the soil surface. The relative surface soil moisture m_s, in degree of saturation, can be calculated with the following equation:

$$\sigma^0(\theta, t) = \sigma^0_{dry}(\theta, t) + m_s(t)[\sigma^0_{wet}(\theta, t) - \sigma^0_{dry}(\theta, t)] \qquad (2.9)$$

where θ is the incidence angle, t is the time, σ^0_{dry} is the dry reference, that is the backscatter that one would obtain under completely dry soil conditions in decibels, σ^0_{wet} is the wet reference, which is the equivalent to the dry reference, but for saturated soil conditions. The term in brackets is referred to as sensitivity S of the backscattering coefficient σ^0 to changes in soil moisture:

$$S = \sigma^0_{wet}(\theta, t) - \sigma^0_{dry}(\theta, t) \qquad (2.10)$$

Hereafter, the determination of the different parameters in equation 2.9 will be outlined. In each subsection, first an overview of the original TU-Wien method developed for scatterometers is given and in an additional paragraph the adapted version of the algorithm for Envisat ASAR and Sentinel-1 is explained.

2.2.1 Incidence Angle Normalization of Backscatter Measurements

Microwave sensors usually scan the Earth's surface in a certain incidence angle range. Hence, the backscatter measurements σ^0 at different locations are taken at different incidence angles. The intensity of the backscatter signal strongly depends on the incidence angle, which results in decreasing backscatter values for increasing incidence angels and vice versa. Thus, σ^0 measurements taken at different incidence angles cannot be compared directly and need to be normalized to a certain reference angle.

In the TU-Wien method for scatterometers, all σ^0 are therefore transformed to a reference angle of $40°$. Equation (2.11) shows a second order polynomial, which was found to be adequate to model the incidence angle behaviour of σ^0 [Wagner, 1998].

$$\sigma^0(40,t) = \sigma^0(\theta,t) - \sigma'(40,t)(\theta - 40) - \frac{1}{2}\sigma''(40,t)(\theta - 40)^2 \qquad (2.11)$$

The parameters of this model, referred to as slope $\sigma'(40,t)$ and curvature $\sigma''(40,t)$, are the first and second derivative of $\sigma^0(\theta)$. Due to the special antenna arrangement of ERS and Metop (see 3.3.1) it is possible to determine the slope and curvature values from simultaneous multi-incidence angle observations. These two parameters are very sensitive to surface structure and vegetation growth. For a smooth surface with no vegetation, σ^0 decreases faster with increasing θ (specular reflection, see 2.1.2), which results in low negative σ' values. Rough surfaces and vegetation have higher σ' values (diffuse scattering), which results in a not so steep decline of σ^0 with respect to θ (see Figure 2.6). Hence, the slope values represent the variations of vegetation canopies within a year, therefore vegetation growth/decay has to be taken into account when normalizing σ^0 values.

SAR   Due to the missing capability to measure backscatter at different incidence angles instantaneously, modelling of seasonal slope effects is not easily possible in the case of ASAR and Sentinel-1. During each overpass, they acquire only one backscatter measurement at a time for one location, hence it is not possible to detect changes in the slope parameter, which refers to vegetation changes. However, for the incidence angle range of ASAR GM ($20°$ to $40°$), Pathe et al. (2009) showed that the slope parameter is constant in time, because in this incidence angle range changes in backscatter due to vegetation growth are much smaller, than changes due to soil moisture. Hence, a linear model is sufficient to describe the incidence angle variation. Due to the similar incidence angle range, a constant slope parameter is also adapted to ASAR WS and Sentinel-1. The following equation is the adapted equation for modelling the incidence
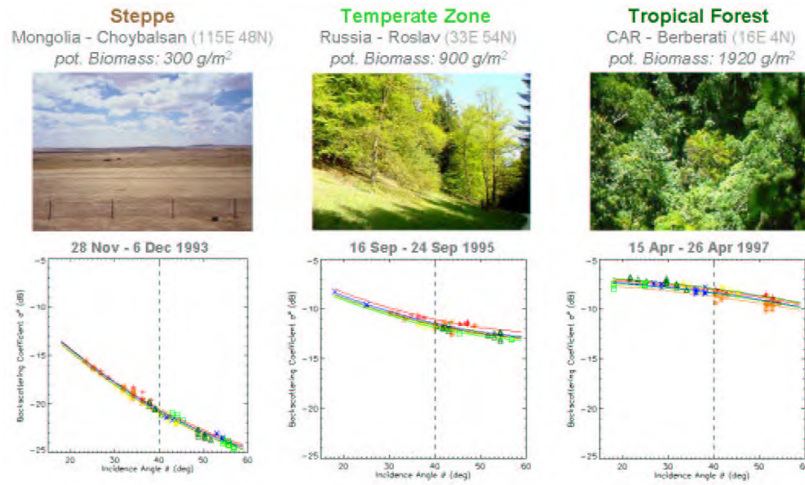
Figure 2.6: *Incidence angle dependency of backscatter over three different surfaces, high vegetation growth results in higher slope value [Scipal, 2002].*

angle behaviour in the SAR algorithm. The σ^0 measurements are extrapolated to a reference angle of $30°$ using the constant slope parameter β.

$$\sigma^0(30,t) = \sigma^0(\theta,t) - \beta(\theta - 30) \tag{2.12}$$

Figure Figure 2.7 shows the slope parameters calculated from ASAR WS data. It is noted that here the value range of the WS slope parameter is between 0 and -0.3. Green represents areas with slightly higher values, which indicates areas with dense vegetation (see figure Figure 3.9) or diffuse scattering mechanisms. Bright green areas represent lower slope values and smooth surfaces where specular reflection dominates.
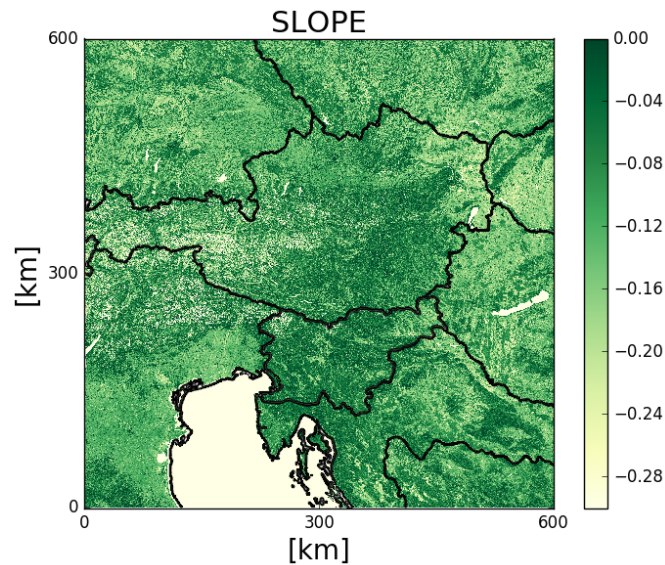
Figure 2.7: *Slope parameter calculated from ASAR WS data.*

2.2.2 Dry and Wet Reference Determination

Before one can determine the dry and wet reference, it has to be stated once again that fully grown vegetation has a large impact on the measured backscatter and furthermore on the soil moisture retrieval. At larger incidence angles, the total backscatter is dominated by vegetation scattering, whereas at smaller incidence angles radiation may penetrate through the dense vegetation and the total acquired backscatter is influenced by the surface scattering term (see Section 2.1.2).

For scatterometers and their incidence angle range, Wagner (1998) stated that there exist so-called "crossover" angles, one for dry and one for wet conditions (dry crossover angle θ_{dry} can be found at 25° and the wet crossover angle θ_{wet} at 40°, Wagner et al. (1999)). At these angles, it is assumed that the vegetation effect in the total backscatter is minimal and backscatter changes are only caused by soil moisture changes. Referring to scatterometers, this can be exploited to get the historically driest and wettest reference of soil moisture. Vegetation is assumed to have no impact on the total backscatter at these angles, therefore the normalized backscatter measurements are extrapolated to the dry crossover angle θ_{dry} and furthermore the dry reference is determined by calculating the mean of the n-lowest backscatter values. Due to the fact that the reference angle θ_{ref} and the wet crossover angle θ_{wet} are both equal 40°, there is no need to extrapolate the σ^0 values to get the wet reference.

SAR Due to the simplification that for the incidence angle range of ASAR, changes in backscatter are mainly due to soil moisture changes, it is not possible to extrapolate the σ^0 measurements to the dry and wet crossover angle. According to Pathe et al. (2009), the dry reference σ^0_{dry} and the wet reference σ^0_{wet} can be calculated with following equations:

$$\sigma^0_{dry}(30) \approx \frac{1}{N_{dry}} \sum_{i=1}^{N_{dry}} \sigma^0_i(30) \tag{2.13}$$

$\sigma^0_i(30)$ are sorted in ascending order and the average of the N_{dry}-lowest $\sigma^0_i(30)$ values is the dry backscatter reference. Correspondingly for the wet backscatter reference, by averaging the N_{wet}-highest $\sigma^0_i(30)$ values:

$$\sigma^0_{wet}(30) \approx \frac{1}{N_{wet}} \sum_{i=N-N_{wet}}^{N} \sigma^0_i(30) \tag{2.14}$$

N_{dry} and N_{wet} are calculated for each pixel from historical scatterometer SSM data:

$$N_{dry} \approx N_{GM} \frac{N(m_s < 5\%)}{N_{SCAT}} \tag{2.15}$$

$$N_{wet} \approx N_{GM} \frac{N(m_s > 95\%)}{N_{SCAT}} \tag{2.16}$$

Where N_{GM} is the total number of ASAR GM measurements at that specific pixel location, N_{SCAT} is the total number of ERS soil moisture values m_s at the same location, $N(m_s < 5\%)$ is the number of ERS soil moisture data below 5% and $N(m_s > 95\%)$ is the number of soil moisture data above 95%. The dry and wet reference determination is adapted in the same way to Sentinel-1. Figure 2.8 illustrates the dry and wet references (in [dB]) over the study area calculated from ASAR WS data.
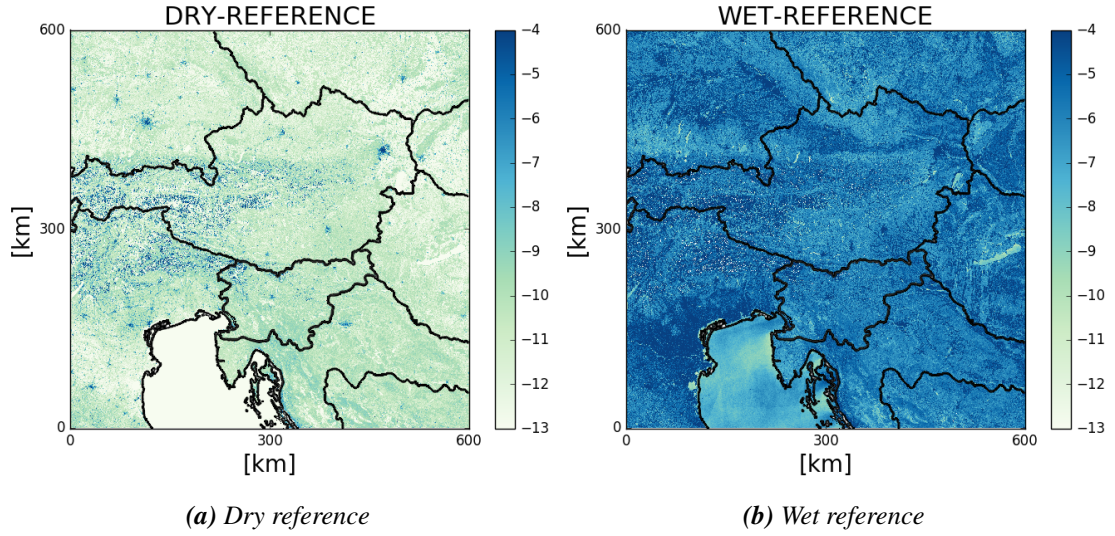
(a) Dry reference   *(b) Wet reference*

Figure 2.8: *Dry and wet reference calculated from ASAR WS data.*

2.2.3 Soil Moisture Retrieval

For ASAR and Sentinel-1 equation 2.9 can be simplified to following change detection model:

$$\sigma^0(\theta, t) = \sigma^0_{dry}(30) + \beta(\theta - 30) + m_s(t) \cdot S \tag{2.17}$$

$$S = \sigma^0_{wet}(30) - \sigma^0_{dry}(30) \tag{2.18}$$

Using the estimated model parameters σ^0_{dry} and σ^0_{wet}, the constant slope value β and the extrapolated backscatter measurements $\sigma^0(30, t)$ (see eq. 2.12), a relative surface soil moisture is retrieved by simply inverting equation 2.17

$$m_s(t) = \frac{\sigma^0(30, t) - \sigma^0_{dry}(30)}{S} \tag{2.19}$$

m_s is scaled to the driest and wettest reference ever recorded, therefore its unit is degree of saturation. Hence, the relative soil moisture content ranges from 0% in a completely dry soil, to 100% in a completely saturated soil.

Chapter 3

Study Area and Data Sets

Spatial reference In order to handle the high resolution SAR data from Envisat and Sentintel-1, Bauer-Marschallinger et al. (2014) designed a new spatial grid, the *Equi7 Grid*, to manage efficiently the archiving, processing and display of high resolution raster data. It is a spatial reference system for the entire Earth, that consists of seven planar subgrids, one for each continent. The coordinates are defined by individual realisations of the Equidistant Azimuthal projection and are referenced to the ellipsoidal World Geodetic System (WGS) 84 datum. Each of the seven subgrids is independently divided into square tiles. To meet the different requirements of low and high spatial resolution, three different levels of tilings are available. For this study the tiling level 'T6' was used, with an tile extend of 600 km and a pixel sampling of 500 m, resulting in 1200 x 1200 pixel.

Study Area Due to the current availability of Sentinel-1 data at the TU-Wien archive, it was only possible to do a proper evaluation over the 'E048N012T6' tile in central Europe (red square in Figure 3.1). As already mentioned, this tile has a spatial coverage of 600 km x 600 km and extends from approximately 10° to 18° of eastern longitude and from 40° to 50° of northern latitude. So it almost covers whole Austria, Slovenia, the north of Italy, the south of Germany and some parts of the Czech Republic, Hungary, Slovakia and Croatia. Regarding topography, great parts of this study area is dominated by the Alps, which cover the whole eastern and central part. In the south-west is the Po Valley, which is broadly divided into a upper, drier part, and a lower, very fertile and well irrigated part. Hence, it is mostly used for agricultural purposes. Also the eastern and south-eastern part of the study area is dominated by agricultural areas, which is called the Pannonian Basin. The Alpine foothills and the highlands of the Bohemian Massif dominate in the north. The land cover types are shown in greater detail in Figure 3.9. The climate in the south-eastern part of the study area is mainly of Mediterranean type, whereas
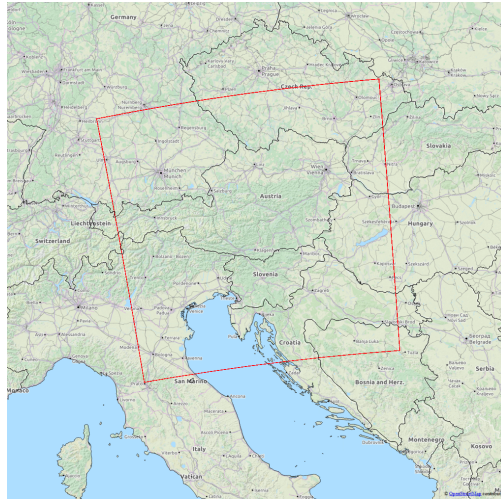
Figure 3.1: *The red square represents the study area (in Pseudo Mercator projection, EPSG:3857)*

the rest is predominated by continental climate. The high-altitude areas in the Alps have a high average rainfall of 2000 mm per year. In the Po Valley precipitation is moderate, with an average of 650 to 1000 mm per year, typically with two maxima in spring and autumn and two relative minima in winter and summer. Figure 3.2 shows the mean precipitation in Austria from 1971 - 2000 and also gives a good impresion of how the Alps influence the climate in this area.
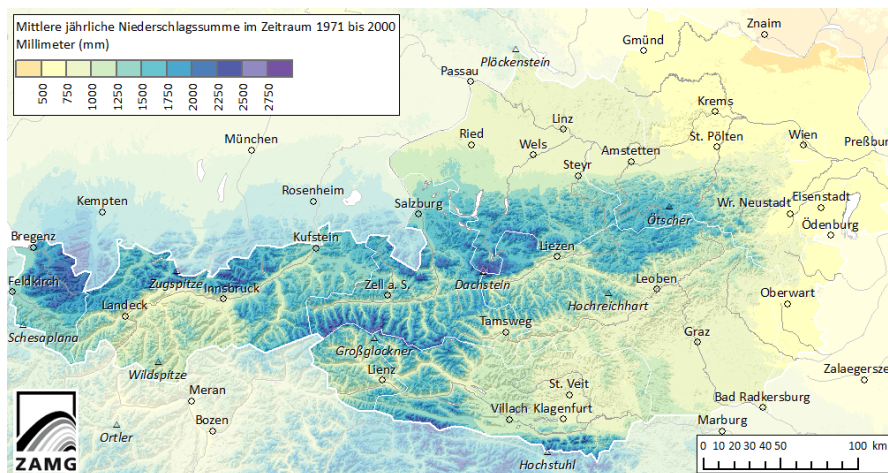

Figure 3.2: *Mean yearly rainfall over Austria (from Hiebl et al. (2011))*

3.1 Envisat ASAR

On March 1, 2002, the European Space Agency (ESA) launched the satellite Envisat into a sun-synchronous polar orbit. Until the unexpected loss of contact with the satellite on April 8, 2012, Envisat circled the Earth at an altitude of about 800 km with a nominal repeat rate of 35 days. With 10 instruments aboard and eight tons it was the largest civilian Earth observation mission so far. One of the instruments was the Advanced Synthetic Aperture Radar (ASAR), an active microwave system operating in C-band at a central frequency of 5.331 GHz. ASAR was able to acquire backscatter data in five different imaging modes with different settings, with respect to spatial resolution, radiometric accuracy and polarizations. To meet the needs of the user, ASAR modes were exclusive modes, which operated on user requests. However, if no other mode was requested, than the global monitoring mode is activated by default. This acquisition strategy led to a quasi arbitrary coverage in the different modes during different times [Wagner et al., 2012].

Global Monitoring Mode (GM)   The GM mode is the so-called background mode, which means it is only active when no data from other modes are requested. Thus, the GM mode provides a higher temporal coverage on a global scale, than other modes. It provides low resolution (1 km) images over a 405 km swath at HH or VV polarization.

Wide Swath Mode (WS)   The WS mode is used for medium resolution (150 m) images over a 405 km swath also in HH or VV polarization. When compared with the GM mode, the WS mode offers a better performance in terms of radiometric resolution, but at the costs of a lower temporal resolution and reduced spatial coverage [Gruber et al., 2013]. On a global scale, GM surpasses WS in terms of temporal resolution and spatial coverage, but if one considers the study area in central Europe, than the WS mode provides data almost as often as the GM mode.

Figure 3.3 shows all available images from ASAR GM (Figure 3.3a) and WS (Figure 4.4a) over the study area from 2004 until 2012. Although the GM mode was the background mode of ASAR, the number of available images for GM and WS is almost even over the study area. Table 3.1 summarizes the characteristics of the ASAR WS and GM mode.
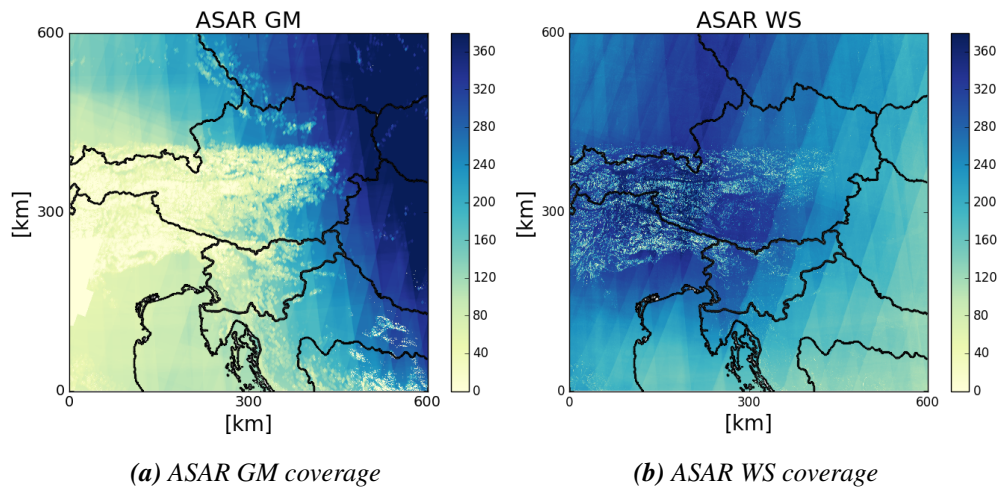
(a) ASAR GM coverage   *(b) ASAR WS coverage*

***Figure* 3.3:** *Number of available images of ASAR GM and WS (2004 - 2012)*

3.1.1 ASAR SSM

For both modes, the global monitoring mode and the wide swath mode, SSM datasets were retrieved using the adapted TU-Wien change detection algorithm from Pathe et al. (2009). It represents the surface soil moisture in the upper layer of the soil (0 - 3 cm) at a spatial resolution of 1 km (with a 500 m sampling). For the GM mode, 898 images are available from December, 2004 till April, 2012, for the WS mode, 986 images from July, 2005 till April, 2012. Figure 3.4 shows the soil moisture of GM and WS for two different days in September, 2009, illustrating the different noise level of the GM and WS data.
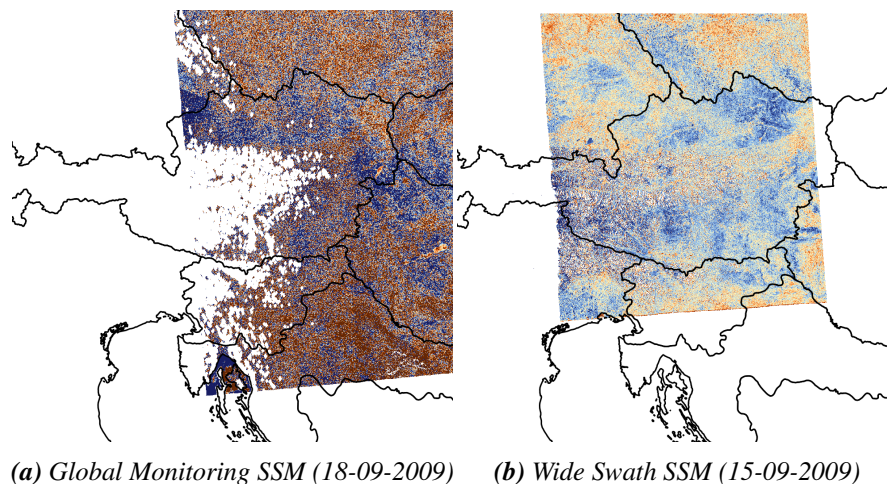

(a) Global Monitoring SSM (18-09-2009)   *(b) Wide Swath SSM (15-09-2009)*

***Figure* 3.4:** *Surface Soil Moisture of Envisat ASAR GM and WS mode*

3.2 Sentinel-1

The Sentinel-1 mission is a part of the Copernicus program of ESA and the European Comission (EC). The Sentinel-1 mission consists of two-satellites sharing the same orbit, each at 693 km mean altitude and with a 180 degree phasing difference [Torres et al., 2012]. Each satellite carries a C-band SAR instrument (5.405 GHz), providing continuous all-weather and day-and-night imagery. The first satellite, Sentinel-1A, was launched into its sun-synchronous, near polar orbit in April, 2014. One single satellite provides full coverage over Canada and Europe every four days and a global coverage every 12 days [Dostálová et al., 2014]. Sentinel-1 offers four different modes for data acquisition, but only the Interferometric Wide Swath (IW) mode is the operational mode and most of the time used, the others are available for emergency requests. The IW mode supports operation in different polarizations (HH, VV, HH + HV, VV + VH) with a spatial resolution of 5 x 20 m over a swath width of 250 km (see also Table 3.1). On April 25, 2016 ESA launched the second Satellite, Sentinel-1B, into its orbit. Both satellites together are expected to cover the Land Masses globally every six days, with almost daily coverage over Europe and Canada [Snoeij et al., 2011]. The number of available images for Sentinel-1 is plottet in Figure 3.5.
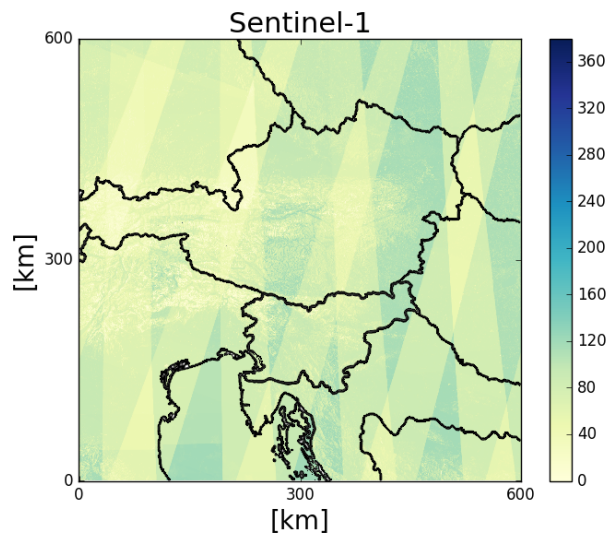

***Figure* 3.5:** *Available Sentinel-1 images from October 2014 until January 2016*

3.2.1 Sentinel-1 SSM

Due to the similar sensor characteristics of ASAR and Senintel-1, the adapted TU-Wien change detection method from Pathe et al. (2009) was also used for the SSM retrieval with Sentinel-1. Due to the lack of historical data (Sentinel-1A is only operating for 18 months), the parameters (slope, dry and wet reference), derived from historical ASAR WS data, were used for the retrieval. Again the soil moisture represents the upper layer of the soil (0 - 3 cm) at a spatial resolution of 1 km, with a 500 m sampling. In total, 1542 Sentinel-1 images were processed over the study area from October 2014 till January 2016. Figure 3.6 shows the Sentinel-1 SSM, it was composed from 5 single images.
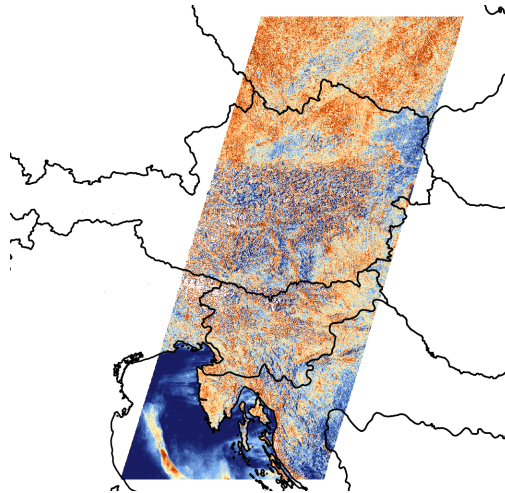

Figure 3.6: Sentinel-1 SSM (20-09-2015)

		Global Monitoring	**Wide Swath**	**Sentinel-1 IW**
Frequency	[GHz]	5.331	5.331	5.405
Spatial resolution	[m]	1000	150	20
Radiometric resolution	[dB]	1.2	0.6	0.3
Temporal Resolution		Irregular, typically 4 to 7 days	Irregular, dependent on acquisition plan	3-6 days Europe, Global 6-12 days (1 satellite)
Spatial coverage		Global	Global	Global
Polarization		HH	VV (HH)	VV, VH

Table 3.1: The characteristics of the ASAR Global Monitoring mode and Wide Swath mode data and Sentinel-1 IW Swath data.

3.3 Ancillary Datasets

As mentioned above Envisat had an operational lifetime from 2002 till 2012. In 2014, two years after the end of the Envisat mission, Sentinel-1 was launched into its orbit. So there is no overlapping period to compare the performance of both satellites directly. Hence some reference datasets are needed in order to perform an evaluation of the soil moisture datasets of both SAR systems.

3.3.1 Metop ASCAT SSM

ESA and EUMETSAT jointly developed three sun-synchronous Meteorological Operational Platforms (Metop-A, Metop-B, Metop-C). Each satellite has a nominal lifetime in orbit of about five years [Figa-Saldaña et al., 2002]. Metop-A, launched in 2006, is still in orbit and will operate in parallel to Metop-B (launched in 2012) as long as the available capacities bring benefits to the user. Metop-C is planned to be launched in 2018. The Metop satellites are flying in 29 day repeat cycle orbit with a minimum orbit height of 822 km. The Advanced SCATterometer (AS-CAT) is an active microwave sensor operating at 5.255 GHz (C-band) on board of the MetOp satellites. The antenna configuration of ASCAT (see section Section 2.1.4.1) results in high temporal resolution (daily coverage) and in a relative coarse spatial resolution of 25 km, which is sampled to a 12,5 km grid. Due to the different spatial resolution of ASCAT and SAR datasets, all ASCAT SSM data from beginning of 2007 till end of 2015 was resampled to the Equi7 grid. Figure 3.7 shows one ASCAT surface soil moisture swath over the study area.
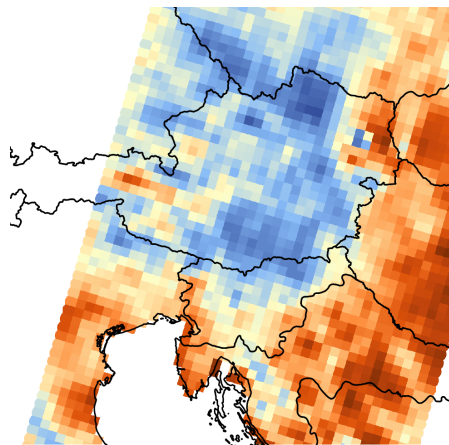

***Figure* 3.7:** *Surface soil moisture from ASCAT in Equi7 grid (21-09-2009)*

3.3.2 GLDAS NOAH SSM

The GLDAS Noah model [Rodell et al., 2004] contains land surface parameters modelled from the Noah model in the Global Land Data Assimilation System (GLDAS). Among others it provides modelled soil moisture information from 1948 till the end of 2015, so it covers the whole lifetime of Envisat and also more than one year of Sentinel-1. The SSM data used, represents the modelled soil moisture in the upper layer of the soil (approximately 0 - 10cm). The data is stored in a regular grid with a spatial resolution of $0.25°$. The temporal resolution is 3 hours, which results in 8 soil moisture values per day, stored in [kg/m^2]. After the calculation of the daily mean, all GLDAS SSM data with beginning of the Envisat lifetime was resampled to the Equi7 grid. Figure 3.8 shows the GLDAS soil moisture of the upper layer of the soil.
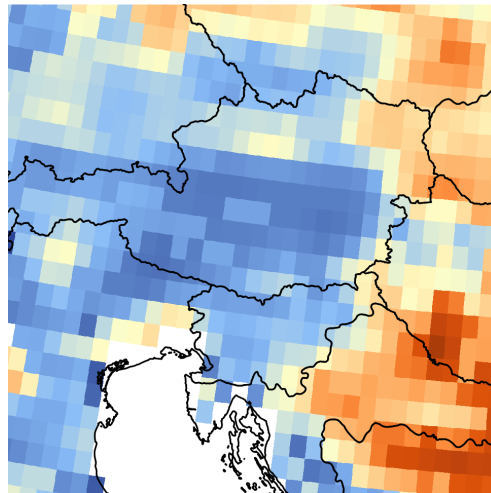

Figure 3.8: GLDAS soil moisture (0-10cm) in Equi7 grid (21-09-2009)

3.3.3 Land Cover Information

The land cover information consulted in this study is retrieved from the Corine Land Cover (CLC) dataset. It is part of the CORINE (Coordination of Information on the Environment) program of the European Union. The objective of the CLC is the provision of a unique and comparable dataset of land cover for Europe. All in all there are 44 classes provided with different land use information. The dataset used in this thesis is the updated version from 2006 with a spatial resolution of 100 m x 100 m. CLC was also resampled to the 'E048N012T6' tile

of the Equi7 grid (Figure 3.9). The different land cover classes are summarized in appendix A.1.
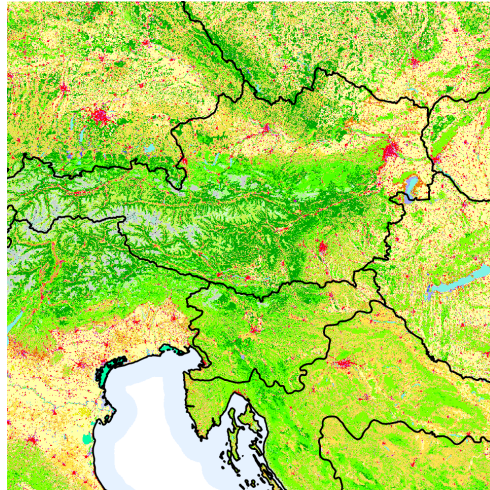

Figure 3.9: Corine Land Cover resampled to the Equi7 grid

Chapter 4

Methodology

Due to the different observation periods of Envisat ASAR (2004-2012) and Sentinel-1 (2014-ongoing) it is not possible to compare the data of these two sensors directly to each other. Hence, to perform an evaluation of the SSM datasets of the two sensors, the reference datasets described in section Section 3.3 are taken. Furthermore, the different lengths of the observation periods, especially the short Sentinel-1 period, and the different number of images per pixel (see Figure 3.3, Figure 3.5)do not allow a direct comparison.

4.1 Visual Inspection

To give a first impression of the data investigated in this study, the different SSM datasets are displayed together with the reference datasets as time series. For all time series a 12 day mean value is calculated. Furthermore for one certain day the available SSM data for the study area is plotted and visually compared to the reference datasets at the same day.

Percentiles are calculated to show the data in a comprehensive way. Percentile is a measure used to indicate the value below which a given percentage of observations of all observations fall [Schönwiese, 2000]. The SSM data are sorted from lowest to highest value and for instance, the 20 percentile represents the value that separates the lowest 20% of the values from the highest 80%. In order to get a deeper impression of the data, different percentiles are calculated per pixel of the SSM time series. For each SAR SSM time series nine percentiles are calculated - also called decile. It is any of the nine values that divide the sorted data into ten equal parts, so that each value represents 1/10 of the sample.

4.2 Time Series Analysis

There are various statistical metrics to quantify the agreement between two datasets. In this study two common bivariate error measures were used: the Spearman correleation coefficient to characterize the temporal agreement of two datasets and the root mean square difference (RMSD) as a measure of the closeness of the SAR SSM datasets to the reference datasets.

4.2.1 Correlation Coefficient

Correlation characterizes a statistical relationship between two datasets. Positive correlation means that if the values of one dataset increase (or decrease), then the values of the second dataset also increase (or decrease). Negative correlation means that the values of one dataset increase and the values of the second dataset decrease and vice versa. However, zero correlation describes two datasets that have no statistical linkage at all. Generally, the correlation between two samples X and Y can be describes as

$$\rho_{(}X, Y) = \frac{Cov(X, Y)}{\sqrt{Var(X)}\sqrt{Var(Y)}} \quad [-1, +1] \tag{4.1}$$

where Cov() donates the covariance and Var() the variance of the two samples. It represents the covariance between the two samples normalized with their respective standard deviation. This coefficient is called *Pearson's Correlation Coefficient* and measures the degree of the linear relationship between X and Y [Von Storch and Zwiers, 2001]. For the variable soil moisture, a normal distribution can not be assumed, thus Pearson's $\rho_{X,Y}$ is not suited. Another correlation coefficients is the *Spearman's Rank Correlation Coefficient*, which estimates the degree of the monotonic relationship and does not require assumptions about the probability distribution of the samples [Mudelsee, 2013]. Spearman's correlation coefficient is calculated similar to Pearson's, but instead of using the actual values, Spearman's uses the rank of the values.

$$\rho = \sum_{i=1} \frac{(x_i - \bar{x})(y_i - \bar{y})}{(x_i - \bar{x})^2 (y_i - \bar{y})^2} \tag{4.2}$$

x_i, y_i and their means $\bar{x}$, $\bar{y}$ do not represent the actual values and their means, instead they represent the ranks (i.e., the sort order index when sorting the data after increasing values) of the values of the samples. That means, the rank correlation coefficient between X and Y is equal to the correlation coefficient between the rank of X and the rank of Y [Mudelsee, 2013].

There exists the probability that the calculated correlation was achieved by coincidence and not by a statistical relationship between the two samples. Such a correlation is called being not significant. The significance of a ρ-value can be tested by computing the test value t in the Student's t-distribution

$$t = \rho \cdot \sqrt{\frac{N-2}{1-\rho^2}} \tag{4.3}$$

where ρ is the correlation coefficient and N is the number of data pairs. Common thresholds for considering a correlation value to be significant are 0.05 or 0.01, that is, there is a 5% or 1% probability that the correlation is a coincidence [Schönwiese, 2000].

4.2.2 Correlation Layer

Before the correlation coefficient can be calculated, each of the SAR datasets - ASAR GM and WS, Sentinel-1 - have to be temporally matched with each of the two reference datasets - ASCAT and GLDAS. That is, within a 12 hour window before and after the SAR timestamp, the nearest timestamp of the reference dataset, which also has a spatial matching, is searched and selected. For those temporally matched time series the Spearman correlation coefficient was computed at each pixel location of the study area (1200 x 1200 pixel). This results in six correlation layers (CL), three per reference dataset that are plotted as maps. Furthermore, the significance value and the number of temporally matched timestamps are stored in separate layers.

It is known that the SSM retrieval algorithm behaves different over certain land cover types. Therefore, the CL is separated into five layers containing different classes from the Corine Land Cover map:

- Agricultural areas and open soils

- Artificial surfaces

- Forests

- Mountains

- Water bodies and wetlands

The detailed sub-classification can be seen in the appendix A.1. These five sub-classes are shown in Figure 4.1. The *agricultural areas and open soil* class is the largest class, it covers exactly half of the study area (50.1%). Among the other four classes, which cover almost the rest of the area (2.5% are within the Adriatic Sea and not assigned to any class), the forest sub-class is the
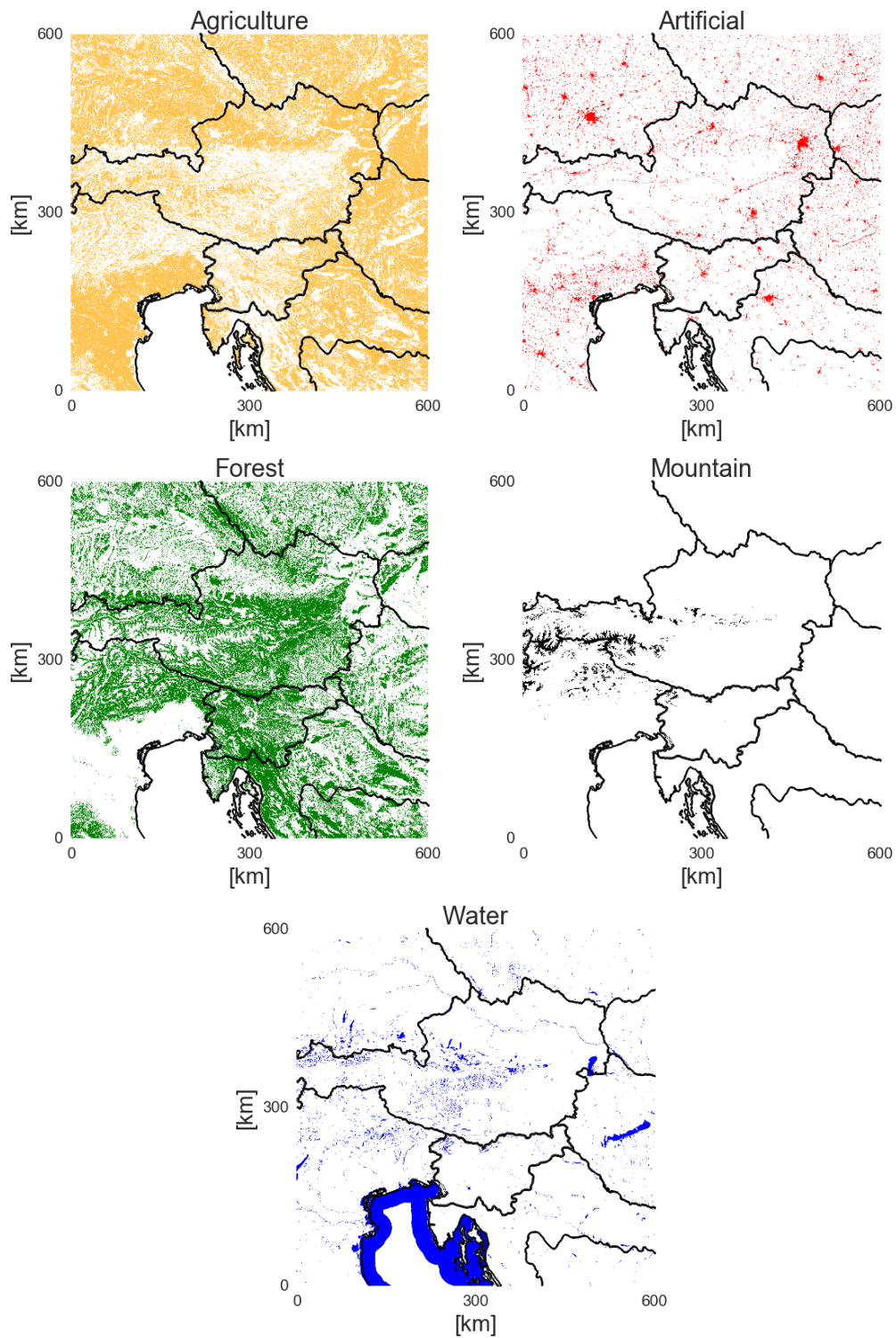
***Figure* 4.1:** *Sub classes derived from Corine Land Cover*

largest one (see Table 4.2). For each of the six correlation layers, the correlation coefficients of these sub-classes are derived and displayed as boxplots.

	Number of Pixels	**Percentage of all Pixels**
Agriculture	721 681	50.1%
Artificial	64 632	4.5%
Forest	495 414	34.4%
Mountain	20 432	1.4%
Water	102 006	7.0%
Not Classified	36 030	2.5%

***Table* 4.1:** *Number of pixel in sub-classes*

4.2.3 Root Mean Square Difference

The RMSD is the square root of the averaged squared differences between two datasets. To remove bias and to overcome the problem of different units (SSM from remote sensing satellites is stored in %, GLDAS in kg/m^2), the mean standard deviation transformation of the reference dataset to ASAR and Sentinel-1 SSM was applied. The resulting RMSD highlights the random errors between the datasets.

$$RMSD = \sqrt{\frac{1}{N} \sum_{i=1}^{N} (X_i - Y_i)^2} \tag{4.4}$$

Similar to the correlation layer, the RMSD is calculated between the reference datasets and ASAR and Sentinel-1, respectively. Furthermore, the RMSDs are plottet as boxplots for each sub-class as described in the previous section.

4.2.4 Correlation Mask

The idea is to generate a mask which only shows locations, where the algorithm for soil moisture retrieval from radar observations is robust, i.e. areas that are sensitive to soil moisture. Assuming that ASCAT is a true reference, setting different thresholds for the CL allows the generation of a logical mask, named Correlation Mask (CMASK). This mask only shows pixel that have a

correlation coefficient higher than the certain threshold. This indicates locations where the SSM datasets show a high (depending on the threshold) temporal agreement with the reference dataset and locations where the algorithm should be robust. Furthermore, the derived CMASK can be compared with the Corine Land Cover dataset. Therefore, the Corine Land Cover is consolidated into two major classes (see Figure 4.2):

- Class 1: *Soil Moisture Sensitive Areas (SMSA)*

- Class 2: *Non Soil Moisture Sensitive Areas (Non-SMSA)*

The first class equals the *agriculture* class from Section 4.2.2. It includes agricultural areas and open soils without dense forests. The second class contains the other four classes from above, it includes artificial surfaces, water bodies, dense forests, mountains, bare lands and rocks. In short, areas that are most likely to be not sensitive to the soil moisture retrieval algorithm. The major assumption is that soil moisture can only be retrieved correctly over open soils and not densely vegetated areas. In this case the CMASK should contain the areas from Class 1, whereas the pixel from Class 2 should be masked out. The amount of correctly masked and unmasked pixel is computed and the quantitative results are presented as confusion matrices.
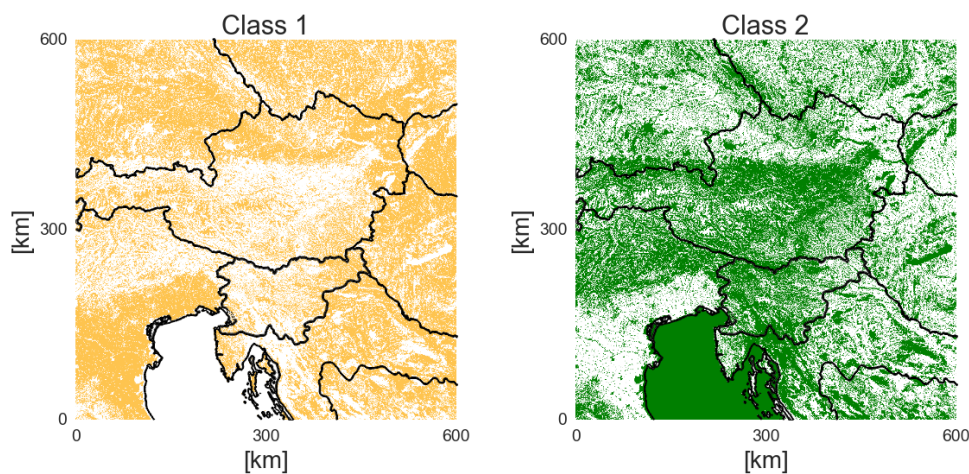
(a) Class 1 for soil moisture sensitive areas *(b) Class 2 for non soil moisture sensitive areas*

Figure 4.2: *Classification for the examination of the sensitivity of retrieval algorithm.*

Confusion Matrix   allows the visualization of the performance of the correlation mask against the two classes from above. The confusion matrix set up for this study is shown in Figure 4.3. Box 1 and box 5 show the amount of correctly unmasked (Class 1) or correctly

masked (Class 2) pixels, respectively. Box 2 shows the amount of erroneously unmasked pixels from Class 2, although they should be masked and box 4 shows the amount of masked pixels from Class 1, although they should be unmasked. The three lower boxes (7, 8 and 9) show the total amount of pixels in Class 1, the total amount of pixels in Class 2 and the total correctly masked or unmasked pixels (sum of the two green squares), from left to right. Figure 4.3. For

Figure **4.3:** *Confusion matrix design*

each correlation layer, CMASKs with thresholds of 0.2, 0.3, 0.4, 0.5, 0.6 are computed. Furthermore, to gather information about the location of the false masked and false unmasked pixels, a confusion map is plotted, which shows the location of the pixels from the boxes 1, 2, 4 and 5 in a map.

4.2.5 Additional Subset Study

As already mentioned at the beginning of this chapter, not only the period for the three sensors is different, also the number of images per pixel area quite different. Table 4.2 shows the mean number of images per pixel, or in other words, the sample size per location of the three sensors. In Figure 4.4, the coverage of the study area for ASAR WS and Sentinel-1 are plotted again. The red square shows a smaller subset of the study area, where both sensors have a similar coverage (second column in Table 4.2). So it seems reasonable to make a subset study for this area, yielding comparable statistics.
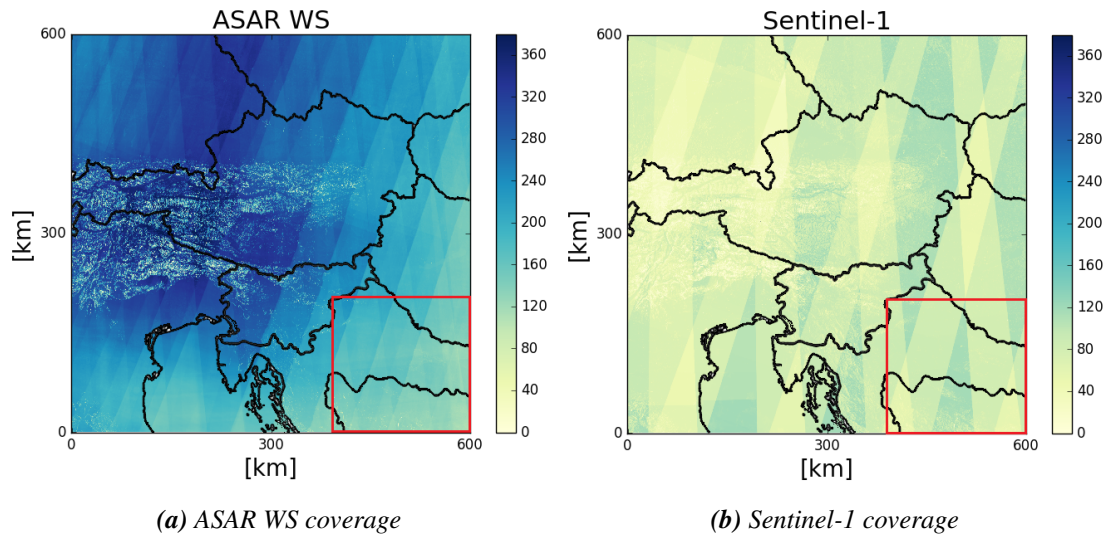
(a) ASAR WS coverage　　　　*(b) Sentinel-1 coverage*

***Figure* 4.4:** *ASAR WS and Sentinel-1 coverage with narrowed study area to get similar sample size.*

	Study area	South-east sub-area
Sentinel-1	72	79
ASAR WS	161	88
ASAR GM	125	130

***Table* 4.2:** *Mean number of images per pixel for the whole study area and for a smaller subset in the south east.*

Chapter 5

Results and Discussion

5.1 Visual Inspection of Datasets

5.1.1 Time Series Representation

The following plots display soil moisture time series of Sentinel-1, ASAR WS and ASAR GM, as well as ASCAT soil moisture as a reference dataset. Four different locations are examined for the comparison of the time series which are displayed in Figure 5.1. Location 1, 2 and 3 are all located in soil moisture sensitive areas, whereas location 4 is located in a densely vegetated area.
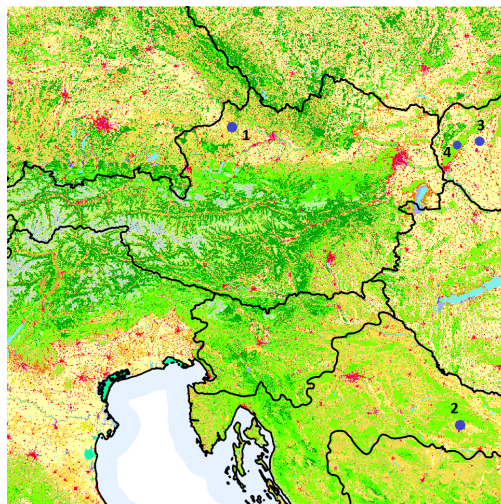

Figure 5.1: *Locations of the examined time series within the Corine Land Cover map. Locations 1, 2 and 3 are soil moisture sensitive areas. Location 4 is a densely vegetated area.*

Figure 5.3, Figure 5.2 and Figure 5.4 all show soil moisture time series of an agricultural area without dense vegetation (locations 1, 2 and 3). Areas like these are very sensitive to soil moisture, which is also very well displayed in these figures. Overall, a good agreement of the different time series is visible. ASAR WS and also Sentinel-1 SSM both follow rather accurately the ASCAT SSM time series, whereas ASAR GM SSM seems to jump back and forth (particularly in Figure 5.3 and Figure 5.2). Especially Sentinel-1 and ASAR WS SSM show the seasonal circles dominating at the study area quite well, with drier periods during summer and wetter periods during winter. Furthermore the different acquisition periods are visible. The ASAR GM and WS mission started in 2005 and ended in 2012, whereas Sentinel-1 acquires data since 2014. Table 5.1 shows the correlation coefficients and RMSD values between the three SAR time series and the ASCAT time series at the different locations. The high correlation values for the soil moisture sensitive areas reflect the visually good agreement of the time series. Also the noisy behaviour of ASAR GM is reflected in Table 5.1. The RMSD values for ASAR GM are always clearly higher than for ASAR WS and Sentinel-1.
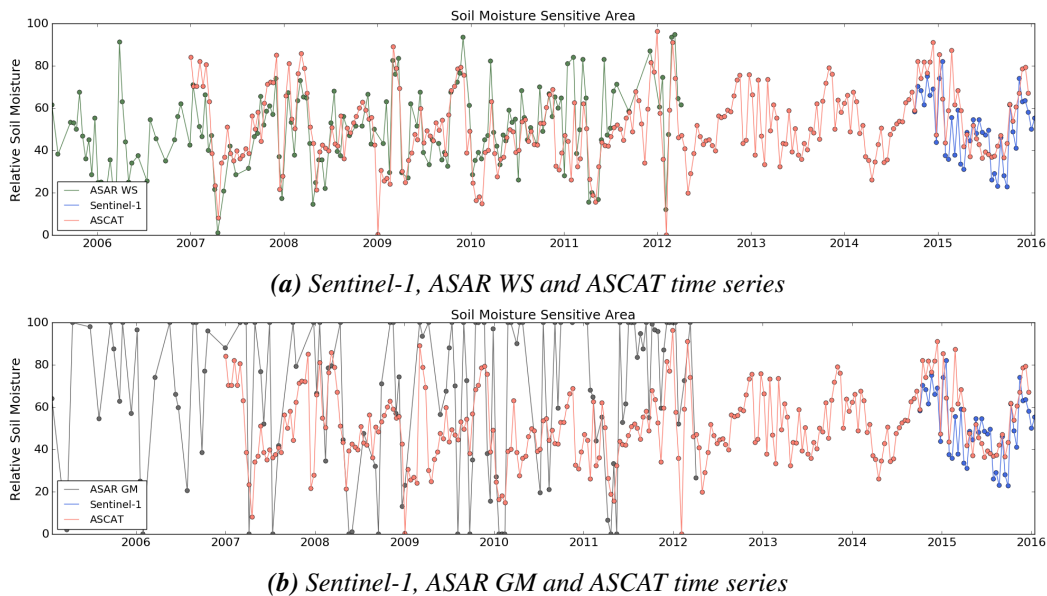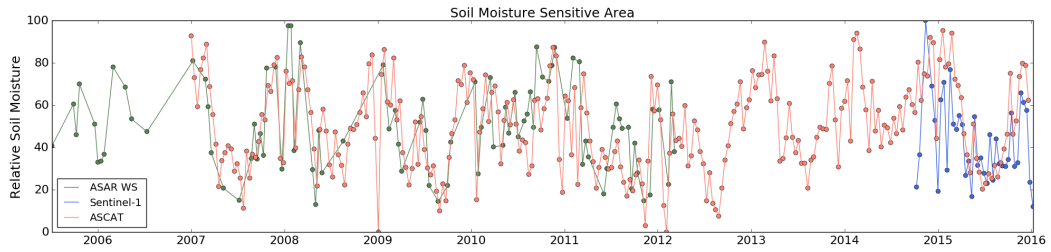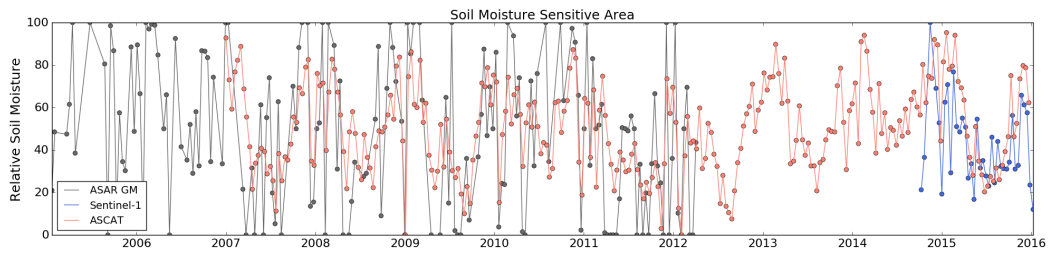

(a) Sentinel-1, ASAR WS and ASCAT time series

(b) Sentinel-1, ASAR GM and ASCAT time series

Figure 5.2: *Soil moisture of different sensors at location 1, ASCAT as a reference.*
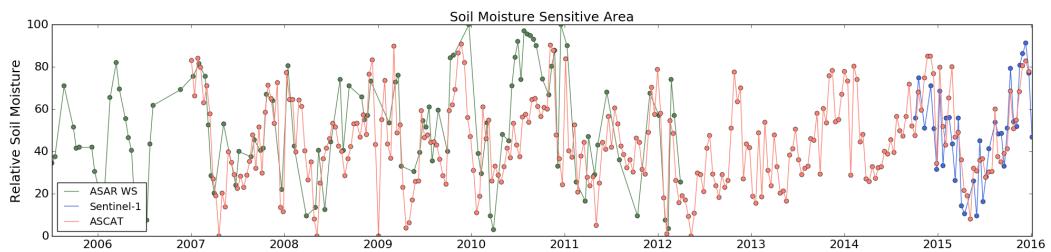
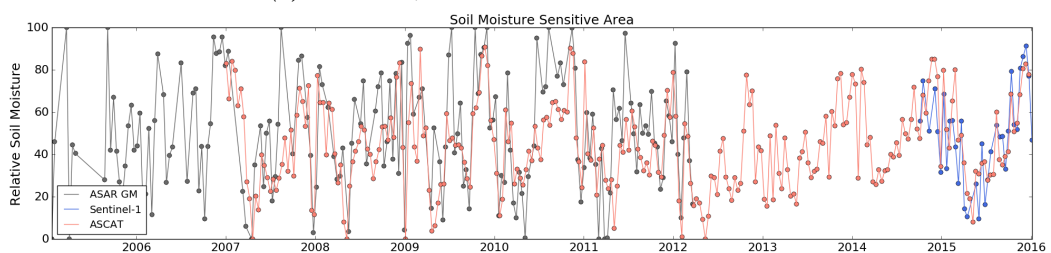*(a) Sentinel-1, ASAR WS and ASCAT time series*

(b) Sentinel-1, ASAR GM and ASCAT time series

Figure 5.3: *Soil moisture of different sensors at location 2, ASCAT as a reference.*

(a) Sentinel-1, ASAR WS and ASCAT time series

(b) Sentinel-1, ASAR GM and ASCAT time series

Figure 5.4: *Soil moisture of different sensors at location 3, ASCAT as a reference.*

		Correlation Coefficient	**RMSD** [%]
Location 1	WS	0.73	16
	S1	0.69	14
	GM	0.56	36
Location 2	WS	0.81	14
	S1	0.70	17
	GM	0.65	35
Location 3	WS	0.77	18
	S1	0.74	20
	GM	0.72	25
Location 4	WS	0.39	26
	S1	0.10	37
	GM	0.12	51

***Table* 5.1:** *Correlation coefficients and RMSD values for different locations and sensors with ASCAT as a reference.*

Figure 5.5 shows soil moisture time series of a densely vegetated area (location 4). At vegetated areas, it is usually difficult to retrieve the moisture content from the soil, due to the high influence of vegetation in the backscattered signal. ASCAT SSM, and to some extent also ASAR WS SSM time series are still able to show a soil moisture signal, whereas Sentinel-1 SSM and especially ASAR GM SSM show no reasonable soil moisture signal any more, both are strongly jumping back and forth. This noisy behaviour for ASAR GM soil moisture was also observed in other studies (e.g. Doubková et al. (2012), Dostálová et al. (2014)). Correlation coefficients and RMSD values are displayed in Table 5.1. It has to be noted that the correlation coefficient for Sentinel-1 and ASAR GM are not significant (p-value higher than 5%), hence no statistical relationship can be assumed for the time series.
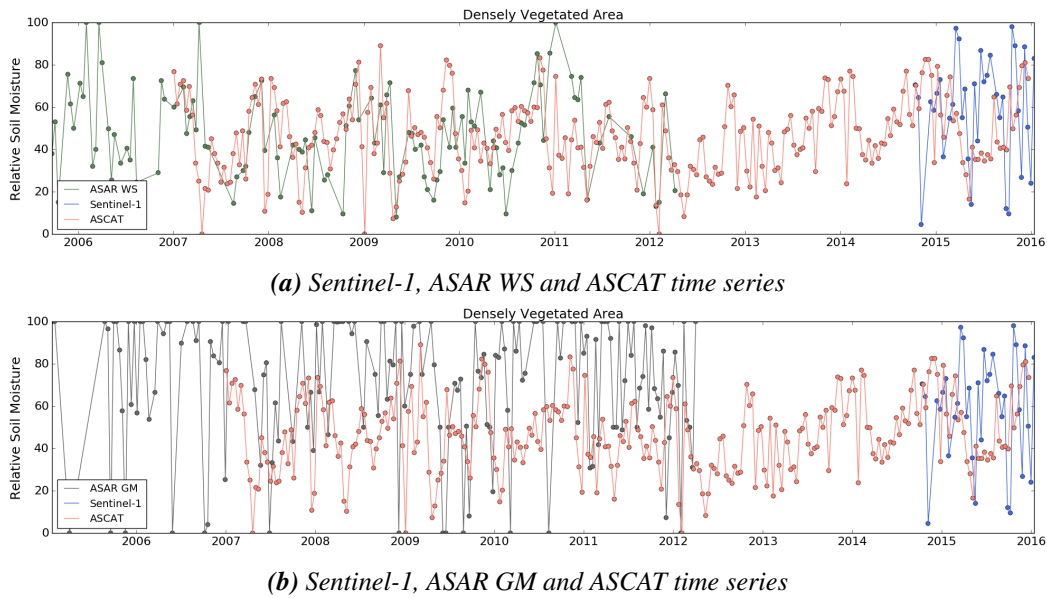
(a) Sentinel-1, ASAR WS and ASCAT time series

(b) Sentinel-1, ASAR GM and ASCAT time series

Figure 5.5: *Soil moisture of different sensors at location 4, ASCAT as a reference.*

5.1.2 Spatial Representation

Figure 5.6, Figure 5.7 and Figure 5.8 show spatial soil moisture patterns from Sentinel-1, ASAR WS and ASAR GM, respectively, compared to ASCAT SSM and GLDAS SSM. The different spatial resolutions of the SSM datasets are clearly visible. The coarse scale ASCAT and GLDAS images only show large-scale trends, whereas especially the ASAR WS and also the Sentinel-1 product clearly resolve distinct dry and wet patterns at the 1 km scale. In the ASAR GM image the large scale patterns from ASCAT and GLDAS can also be seen but are blurred due to the very high noise level.

Figure 5.9, Figure 5.10 and Figure 5.11 show the percentiles of the three SSM datasets at the study area. For all three figures the colour-scale ranges from completely dry (black) to completely wet (white). Sentinel-1 shows a clearly higher contrast in the data, which corresponds to a higher spatial variability, compared to ASAR WS and ASAR GM. It has a much higher skill in resolving spatial patterns, like for instance transitions from urban to rural areas or forests to fields. Again, ASAR GM seems to be blurred when compared to ASAR WS, which is again due to the high noise level of the data.
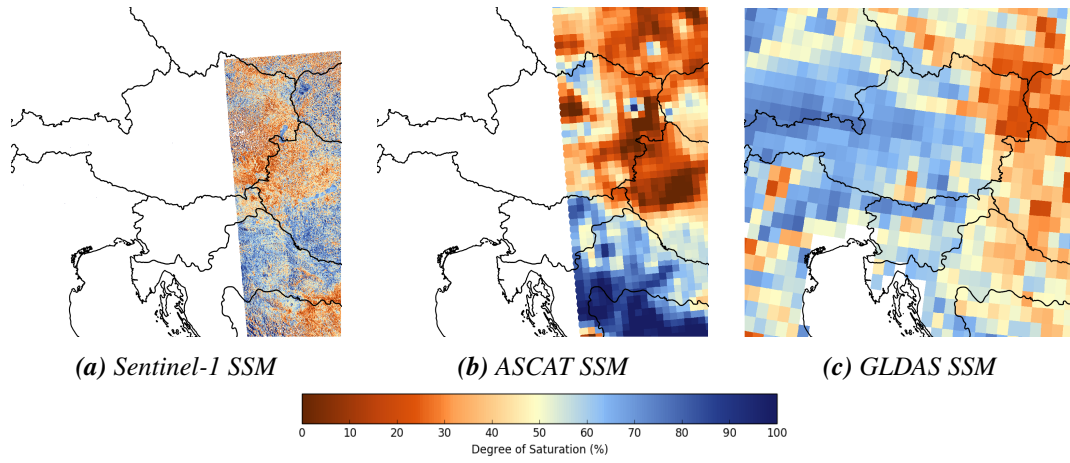
(a) Sentinel-1 SSM *(b) ASCAT SSM* *(c) GLDAS SSM*

Degree of Saturation (%)

Figure 5.6: *Sentinel-1, ASCAT and GLDAS SSM (19-06-2015)*

(a) ASAR WS SSM *(b) ASCAT SSM* *(c) GLDAS SSM*

Degree of Saturation (%)
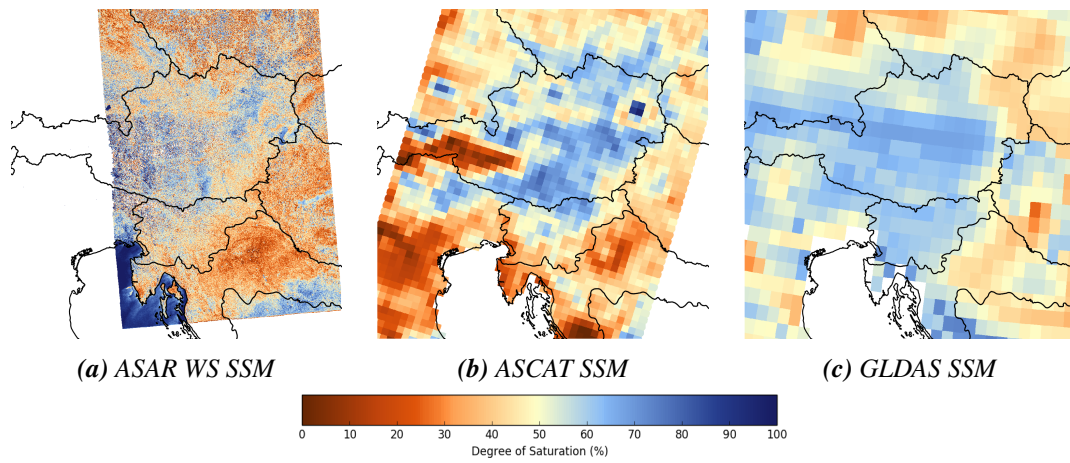
Figure 5.7: *ASAR WS, ASCAT and GLDAS SSM (21-06-2009)*

(a) ASAR GM SSM   (b) ASCAT SSM   (c) GLDAS SSM

Degree of Saturation (%)
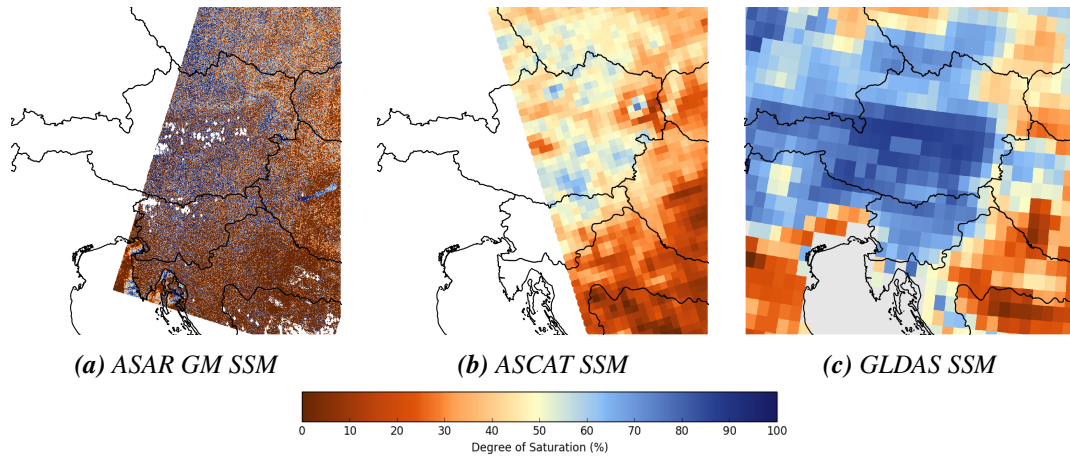
Figure 5.8: *ASAR GM, ASCAT and GLDAS SSM (09-09-2009)*

(a) P-10   (b) P-20   (c) P-30   (d) P-40   (e) P-50

(f) P-60   (g) P-70   (h) P-80   (i) P-90

Degree of Saturation (%)
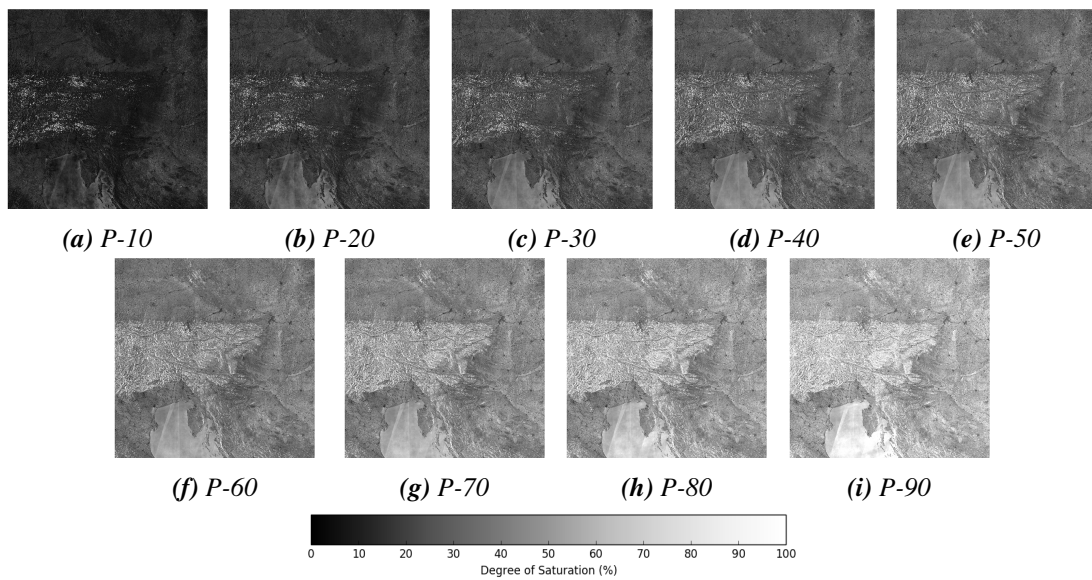
Figure 5.9: *Percentiles of Sentinel-1 SSM.*

(a) P-10 *(b) P-20* *(c) P-30* *(d) P-40* *(e) P-50*

(f) P-60 *(g) P-70* *(h) P-80* *(i) P-90*
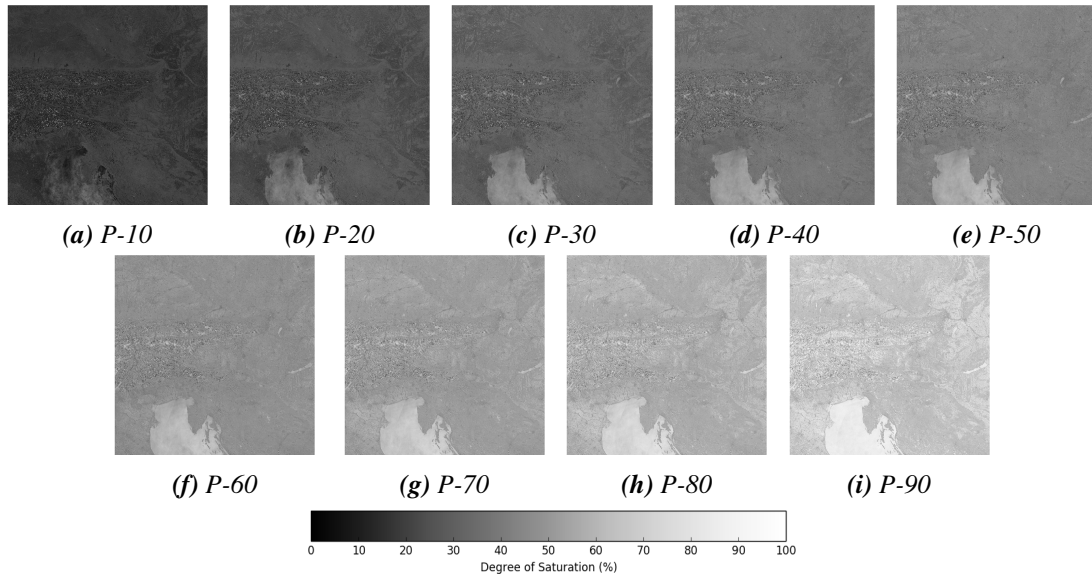
Figure 5.10: *Percentiles of ASAR WS SSM.*

(a) P-10 *(b) P-20* *(c) P-30* *(d) P-40* *(e) P-50*

(f) P-60 *(g) P-70* *(h) P-80* *(i) P-90*

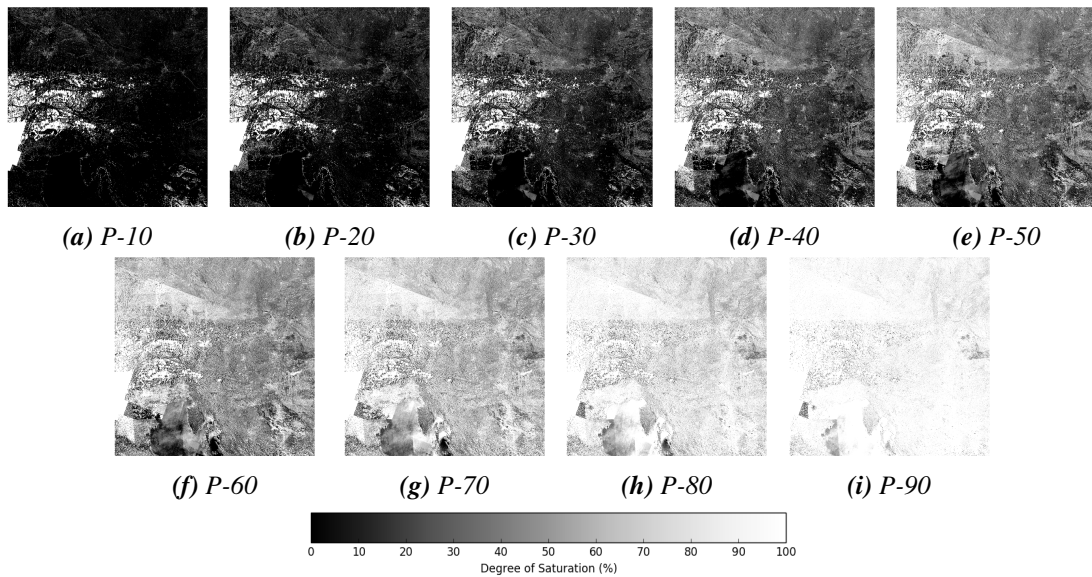**Figure 5.11:** *Percentiles of ASAR GM.*

5.2 Correlation Analysis

The correlation coefficient between ASCAT SSM and Sentinel-1 SSM, ranging from 0 to 1, is displayed in Figure 5.12. The darker the green gets, the higher is the agreement of ASCAT and Sentinel-1 SSM time series at the individual locations. Only correlation values with a p-value lower than 5% are displayed. Figure 5.13 shows the correlation coefficient between ASCAT SSM and ASAR WS SSM with the same color range. The correlation coefficient between AS-CAT SSM and ASAR GM SSM is displayed in Figure 5.14.
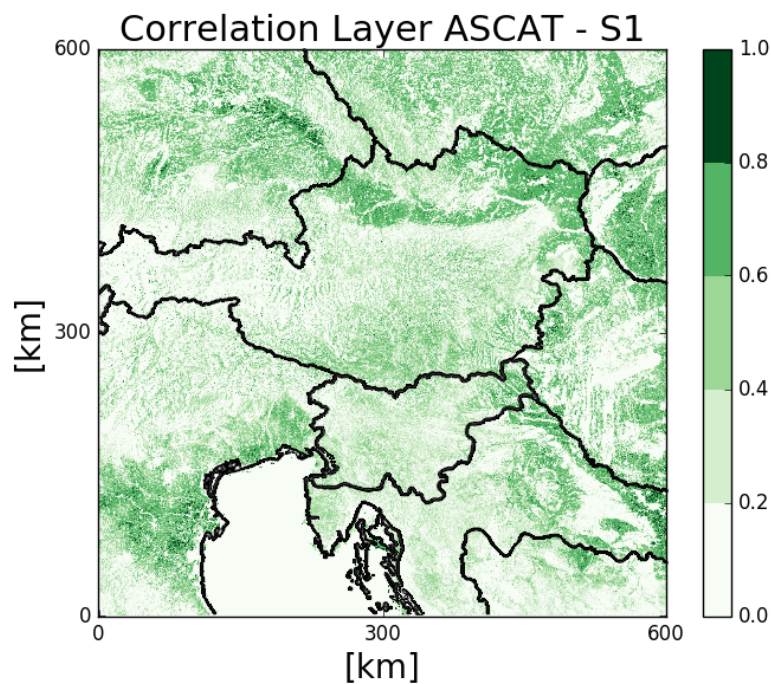

Figure 5.12: *Correlation Coefficients of ASCAT and Sentinel-1*

The correlation coefficient for ASAR GM (Figure 5.14) is clearly lower than for ASAR WS (Figure 5.13), due to an improved spatial as well as radiometric resolution of ASAR WS, which is also caused by the different acquisition strategies (see Table 3.1). Furthermore, the ASAR GM correlation coefficient shows a slightly weaker performance than Sentinel-1 (Figure 5.12). Sentinel-1 only delivers data for 16 months, compared to 8 years of ASAR GM, but still, with respect to quality, the soil moisture data can already compete with ASAR GM SSM. Again, this suggests that the low radiometric resolution of ASAR GM is decreasing the quality of the SSM data.
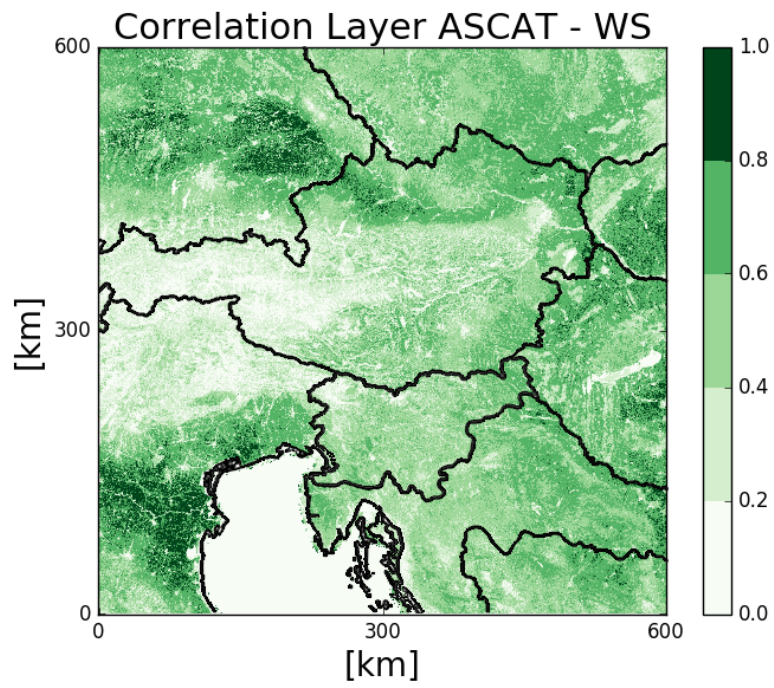
Figure 5.13: *Correlation Coefficients of ASCAT and ASAR WS*
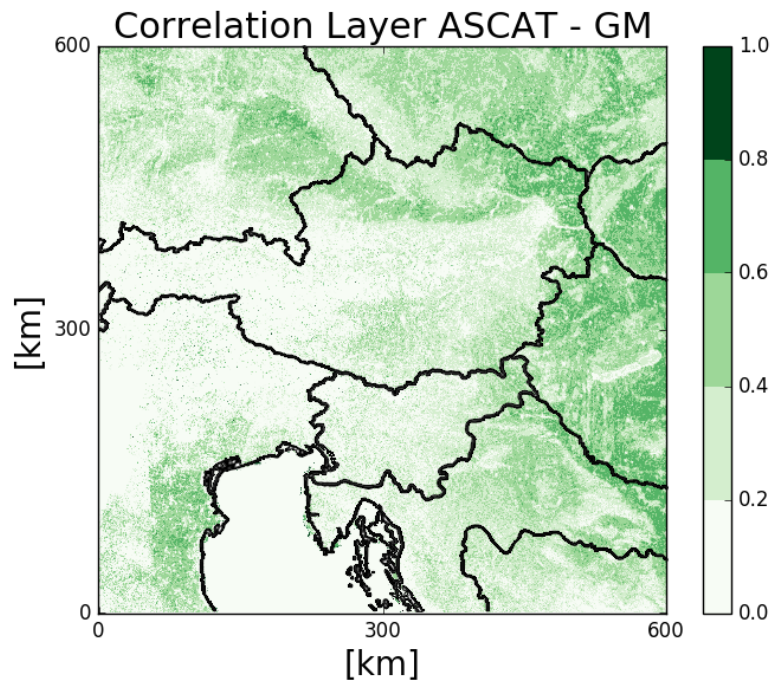

Figure 5.14: *Correlation Coefficients of ASCAT and ASAR GM*

Furthermore the overall pattern of the correlation maps reflects the land cover structures displayed in Figure 3.9. Therefore the correlation results can be interpreted by means of different land cover types (Figure 4.1 shows the five different sub classes). Figure 5.15 shows a boxplot representation of the correlation results for all three sensors stratified by land cover types from the Corine Land Cover. The boxes show the median, 25th and 75th percentiles, the lines represent the minimum and maximum values after outlier removal. For all three sensors the highest correlation coefficients can be found in the 'agriculture' class, which represents agricultural areas and grasslands, i.e. areas without dense vegetation. This class represents exactly half of all pixels of the study area. Especially the large agricultural areas in the Po Valley, in the Pannonian Basin and also in the Alpine Foothills show the highest correlations. The 'forest' class shows a different spectrum of correlation coefficients for the three sensors. Whereas ASAR WS still shows a medium high correlation, ASAR GM and especially Sentinel-1 show a low mean correlation of around 0.3 and 0.2, respectively. The other three classes all show a lower correlation between ASCAT and the three sensors, but due to the low sensitivity to soil moisture in these areas, they are of lower interest.
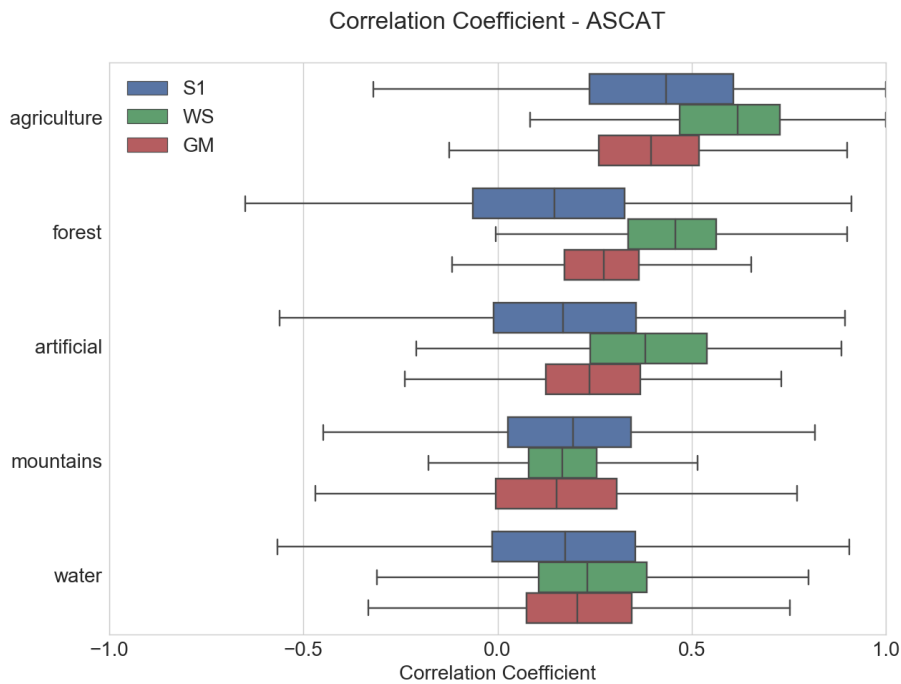

Figure 5.15: Boxplot showing correlations of the different sub classes with ASCAT as a reference.

Figure 5.17 shows the correlation coefficients between GLDAS SSM and Sentinel-1, ASAR WS and ASAR GM, respectively. Compared to the correlation layer for ASCAT, they show generally lower correlations between the different time series. Only for ASAR WS, there are slightly higher correlation coefficients in the Po Valley area and for Sentinel-1 to some extent in the south-east. Also the boxplot representation of the correlation coefficients in Figure 5.16 shows a low correlation level in all five sub classes. This is probably due to the coarse spatial resolution of around 27 km for GLDAS compared to 1 km for the satellite SSM data. This large discrepancy in the spatial resolution assumes that the coarse resolution GLDAS data describes different hydrological signals than the high resolution SAR data. Whereas satellites allow the monitoring of dynamic processes on a regional scale, GLDAS can only capture large-scale events. Due to the low significance of the comparison with GLDAS SSM data, the subsequent experiments were only performed with ASCAT as a reference dataset. Furthermore, Sentinel-1 is only compared to ASAR WS and ASAR GM is neglected in further analyses due to the high noise level in the soil moisture dataset.
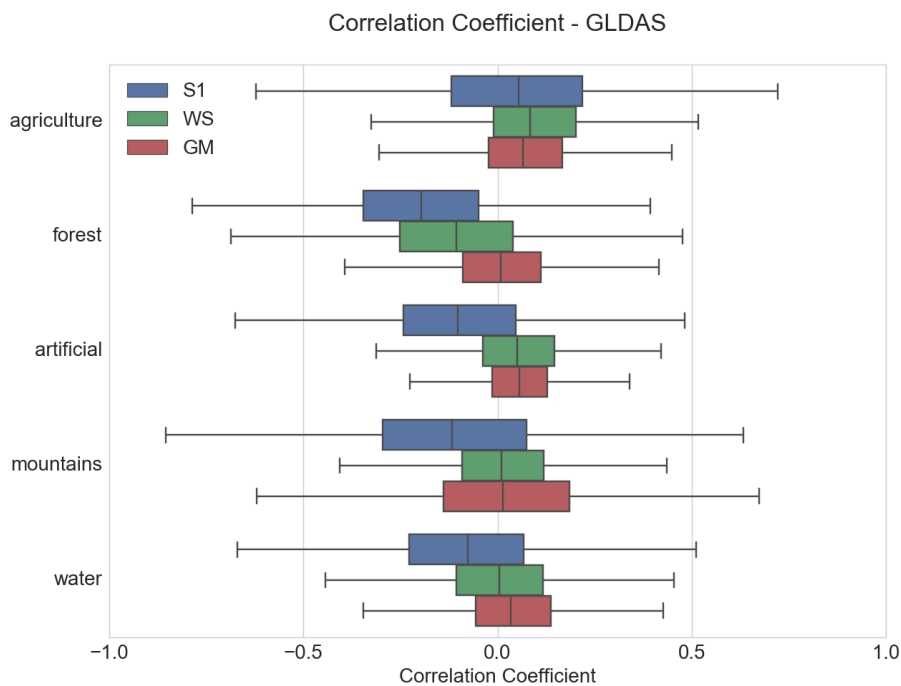

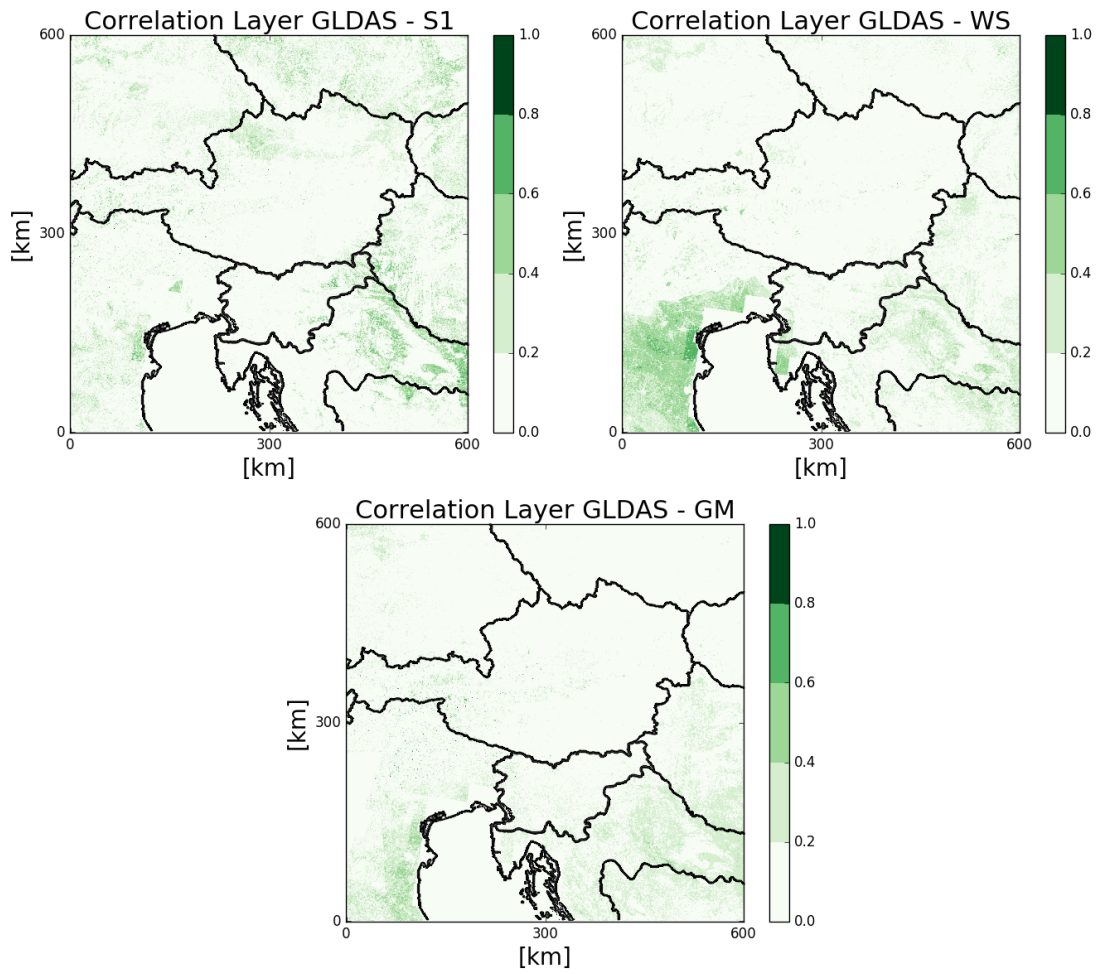**Figure 5.16:** *Boxplot showing correlations of the different sub classes with GLDAS as a reference.*

Figure 5.17: *Correlation layers with GLDAS as a reference*

5.3 RMSD Results Analysis

The RMSD maps for Sentinel-1 (Figure 5.18), ASAR WS (Figure 5.19) and their overall pattern correspond quite well to the correlation maps from the previous section (Figure 5.12 and Figure 5.13). In areas with high correlation coefficients between the datasets, the RMSD values remain lower and in areas with low correlation coefficients the RMSD values are higher. If the two RSMD maps are compared to each other, a clearly better performance of ASAR WS is visible. However, both maps show high RMSD values in the Alpine region, which also corresponds to low correlation coefficients in the correlation maps. Figure 5.19 shows again a boxplot representation of the RMSD values for five different land cover types. The 'agriculture' class shows slightly lower RMSD values for ASAR WS than for Sentinel-1, whereas for the 'forest' class the differences in the RMSD performance are again notable.
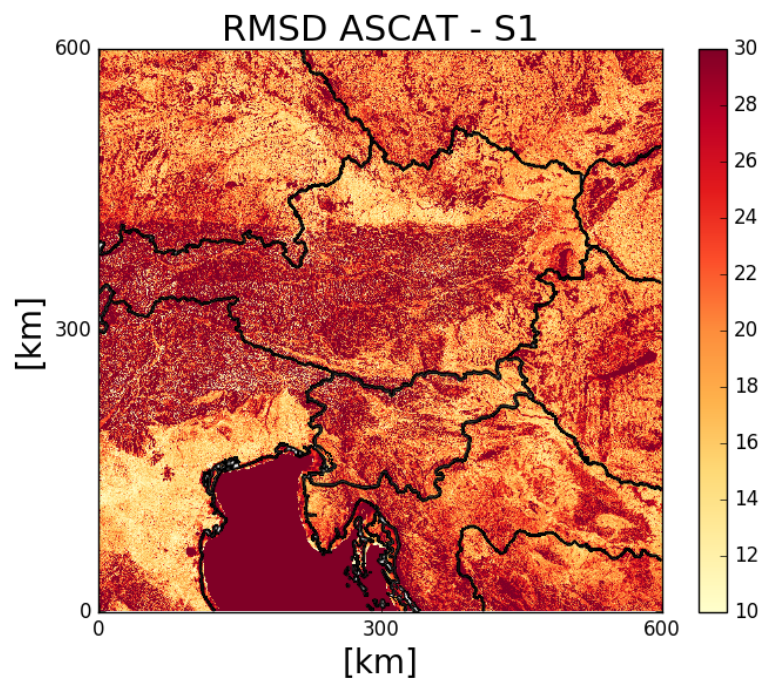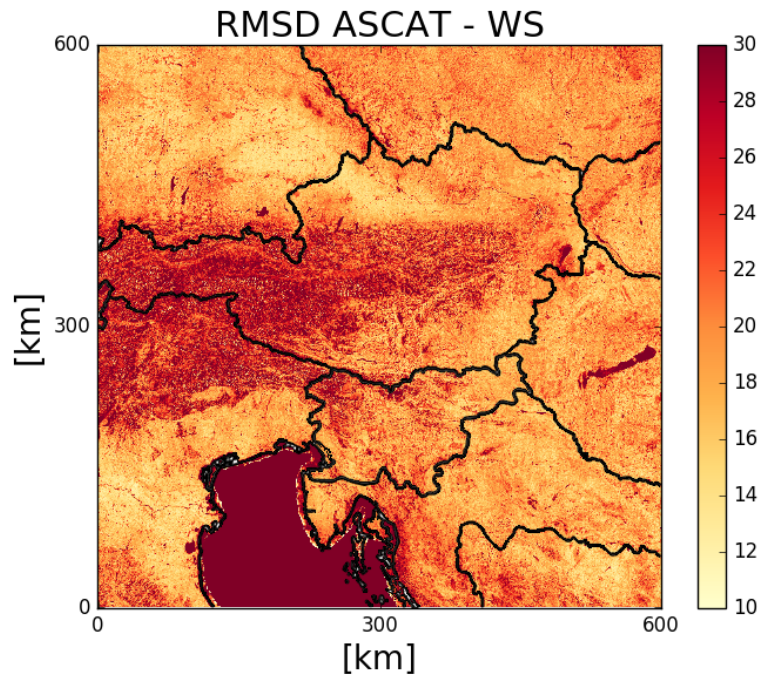

Figure 5.18: *RMSD of ASCAT and Sentinel-1*
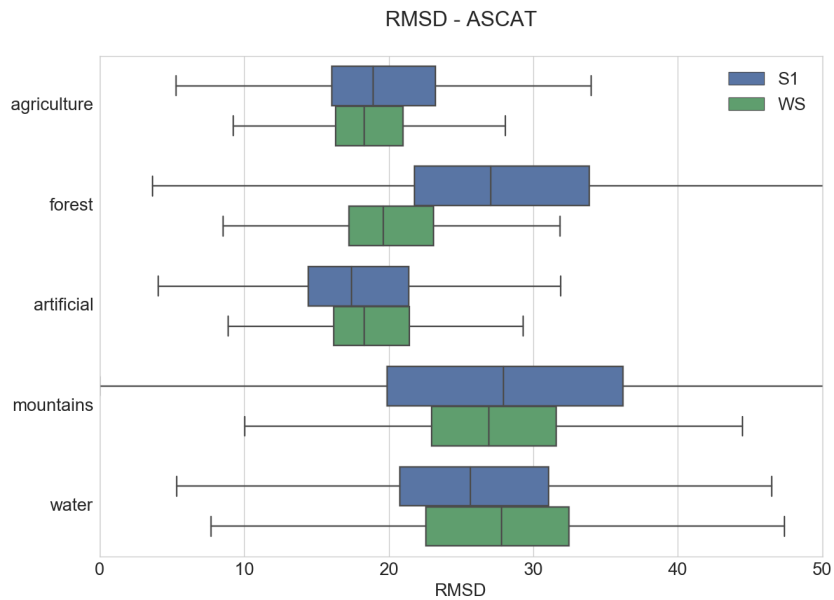
Figure 5.19: *RMSD of ASCAT and ASAR WS*

Figure 5.20: *Boxplot showing ASCAT RMSD of the different sub classes.*

5.4 Discussion of Correlation and RMSD Results

The RMSD and correlation results already suggest that the adaption of the ASAR soil moisture retrieval algorithm to Sentinel-1 is feasible. However, due to the highly improved radiometric resolution of Sentinel-1 it was expected that the soil moisture product already shows a good agreement with the reference dataset. In agricultural and not densely vegetated areas, the correlation of Sentinel-1 is already higher than for ASAR GM but is still not reaching the ASAR WS level. In densely vegetated areas, Sentinel-1 SSM is still not satisfactory. One reason for the weaker performance of Sentinel-1 compared to ASAR WS is the current poor spatial coverage of Sentinel-1 (Figure 3.5). However, as soon as a better Sentinel-1 coverage is established and thus more images are available per pixel location, the performance of Sentinel-1 SSM data is likely to improve. Furthermore, the second Sentinel-1 satellite is going to further increase the data availability and will in order lead to an improved Sentinel-1 SSM product.

5.5 Correlation Mask Results

Various correlation masks with different thresholds were calculated and compared to areas that are sensitive to soil moisture (should be unmasked) and to areas that are not sensitive to soil moisture (should be masked). The major assumption is that soil moisture can only be retrieved correctly over open soils and not densely vegetated areas. It has to be stressed that the CLC map cannot be regarded as the ground truth, because one compares optical data with microwave data. Figure 5.21 shows the confusion matrices, featuring the percentages of the true and false assignings. For Sentinel-1, a minimum threshold of 0.3 delivers the best results and for ASAR WS, a minimum threshold of 0.5. For Sentinel-1, 33.6% of the pixels are correctly unmasked and 37.5% are correctly masked. 12.3% of the pixels are erroneously unmasked although they should be masked and 16.5% are erroneously masked although they should be unmasked. All in all, the share of true assigned pixels is 71.1%. For ASAR WS, 36.5% of the pixels are correctly unmasked and 38.5% are correctly masked. 15.4% of the pixels are erroneously unmasked and 14.6% are erroneously masked. All together, the share of true assigned pixels is 70%. Although the results seem to be similar for both sensors, it must be kept in mind that the chosen thresholds differ, because of the higher correlation level of ASAR WS compared to Sentinel-1. Obviously, the higher the threshold, the higher the share of masked areas and the lower the relative error in the unmasked section, but the higher the relative error in the masked section.
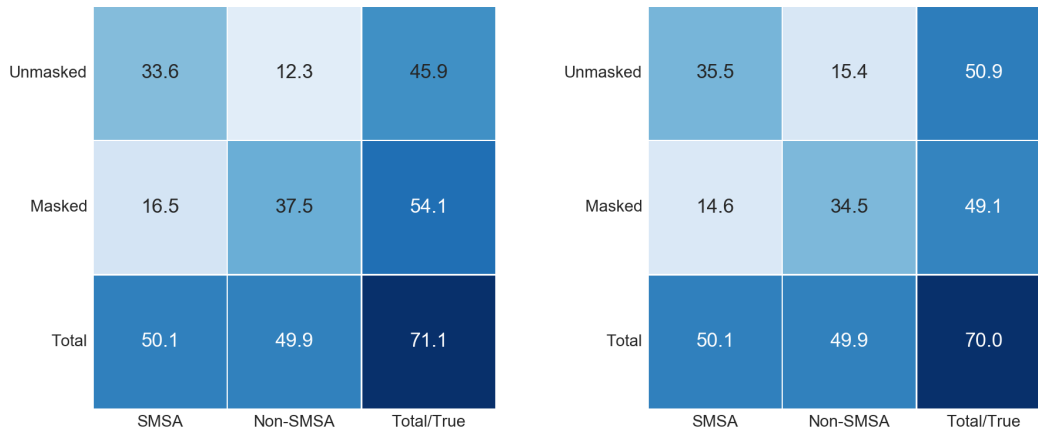
(a) Sentinel-1, with rho = 0.3 *(b) ASAR WS, with rho = 0.5*

Figure **5.21:** *Confusion matrix for Sentinel-1 and ASAR WS vs. ASCAT. For Sentinel-1 the underlying correlation mask was created with a minimum threshold of 0.3 and for ASAR WS with a minimum threshold of 0.5.*

In Figure 5.22 and Figure 5.23, the correctly masked and unmasked pixels as well as the erroneously unmasked and masked (errors of commission or 'SMSA false' and omission or 'Non-SMSA false') are plotted to give an impression where the the correlation mask works well, and where it seems to fail. The correctly masked and unmasked pixels are displayed the colors cyan and dark yellow, respectively. Dark brown and dark green colors represent the erroneously unmasked and masked pixels.

In both maps, an overall good agreement with the classes 'SMSA' and 'Non-SMSA' is visible, having a large share of 'Non-SMSA true' and 'SMSA true' (equivalent to 71.1% of all the pixels for Sentinel-1 and 70% for ASAR WS, as in Figure 5.21). The ASAR WS map appears to be more homogeneous than the Sentinel-1 map, especially the light brown areas representing the 'SMSA' class. For both maps, most errors of commission (dark brown) appear in hilly and mountainous areas, where it is known that the SSM retrieval is prone to errors, but also in densely vegetated areas along the border between the Czech Republic and Germany.

Along the transition zone of the northern Alps (central-west) in the ASAR WS image, the masking appears to be too rigid, which results in errors of omission (dark green). Of course, a big share contributing to 'Non-SMSA true' comes from the Adriatic Sea (central south), which counterbalances the negative impact of the Alps on the statistics in Figure 5.21 to some extent. All in all, the Sentinel-1 map appears to distribute the errors of commission and omission more

randomly across the study area, which could be explained by the low data density of Sentinel-1 and consequently with a lower significance of correlation.
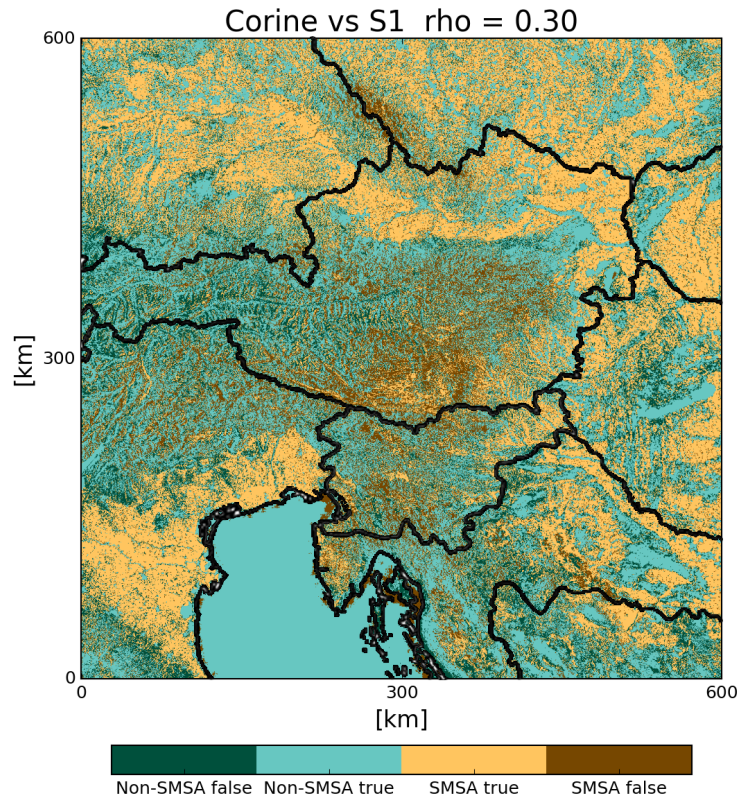

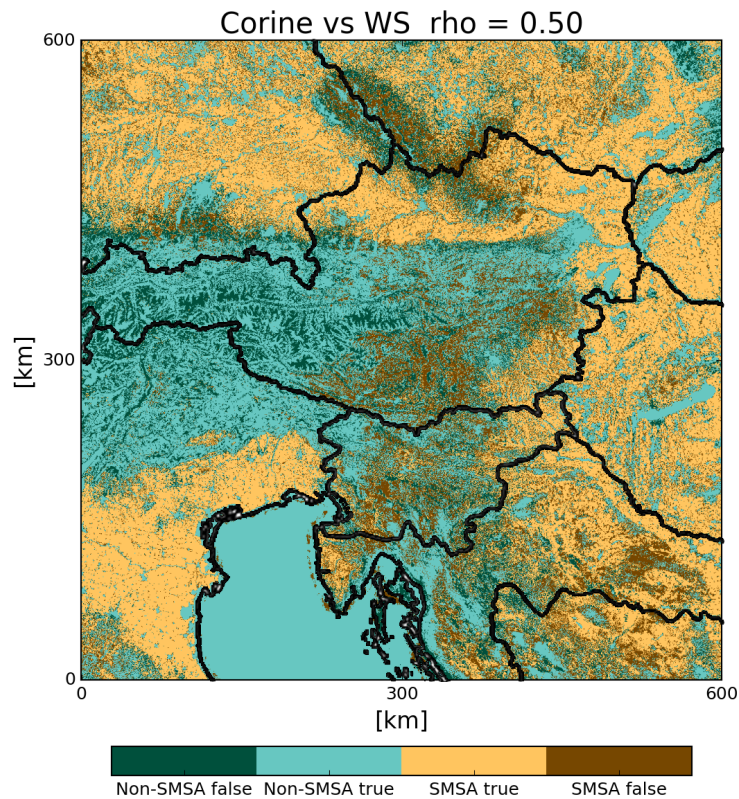***Figure 5.22:*** *Confusion map ASCAT and Sentinel-1*

Figure 5.23: *Confusion map ASCAT and ASAR WS*

5.6 Results of Subset Study

In the previous sections, it is supposed that the smaller sample size of Sentinel-1 compared to ASAR WS (Table 4.2) influences the correlation and RMSD performance. As already mentioned in Section 4.2.5, there is a region in the south-east of the study area where the mean number of available images per pixel for both sensors is similar. It would be expected that in an area with a similar coverage, Sentinel-1 SSM improves due to the improved radiometric resolution. However, Figure 5.24 shows a boxplot representation of the correlation coefficients and RMSD of this area. Although the number of images is now comparable, the correlation coefficients and RMSD values still show no improvement for Sentinel-1 when compared to Figure 5.15 and Figure 5.20. Therefore, one can say that it is not only the different number of available images per location, but may also be the longer period of ASAR WS of 8 years compared to 16 months for Sentinel-1 that influences the performance of Sentinel-1 SSM.
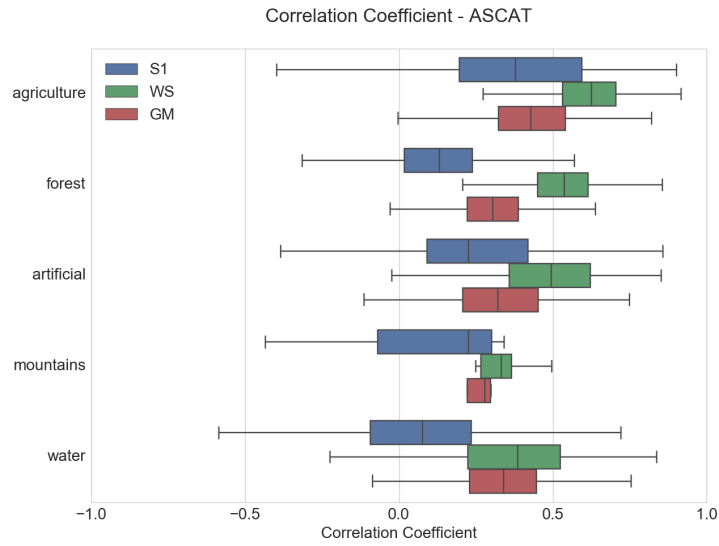
(a) Correlation Coefficient
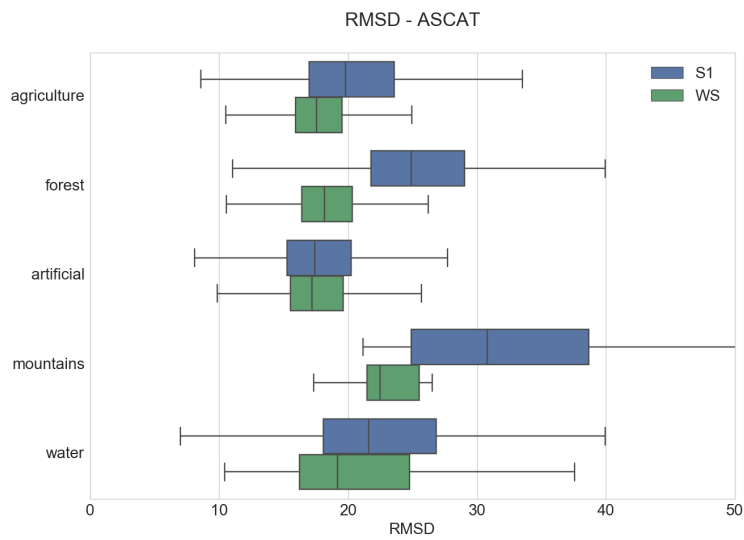
(b) RMSD

***Figure* 5.24:** *Boxplot representation of correlation coefficient and RMSD for south-eastern part of the study area.*

5.7 Discussion

Due to the highly improved radiometric resolution of Sentinel-1, it was expected that the soil moisture product already shows a good agreement with the reference datasets. The visual representation of Sentinel-1 SSM shows a good performance in soil moisture sensitive areas like agricultural areas and grasslands without dense vegetation (Figure 5.2, Figure 5.3, Figure 5.4), but still has problems to deliver satisfactory results over more densely vegetated areas (Figure 5.5).

This assumption was also supported by the correlation and RMSD results analysis. Especially in soil moisture sensitive areas, Sentinel-1 SSM already shows a high correlation to ASCAT SSM, but again there are still problems concerning densely vegetated areas (Figure 5.15).

One reason for the overall weaker performance of Sentinel-1 compared to ASAR WS is the currently low spatial coverage of Sentinel-1, resulting in a low number of images per pixel. However, also a subset study in an area where the number of images per pixel is similar for both, no notable improvement was reached for Sentinel-1 (Figure 5.24). Therefore, it is not only the spatial coverage, but also the short period of 16 months compared to the 8 years of ASAR WS that need to be considered when analysing the correlation coefficient and the RMSD results.

Another reason could be that the Sentinel-1 SAR sensor is calibrated in a different way than the ASAR sensor, resulting in problems when transferring the ASAR WS parameters to the Sentinel-1 soil moisture retrieval algorithm. Although ASAR and Sentinel-1 have a very similar sensor configuration and observe at similar frequencies, it could be the case that the usage of ASAR WS parameters in the Sentinel-1 algorithm results in noisy or biased SSM data. Therefore, a backscatter analysis was performed, where the backscatter coefficients of both sensors were compared to ASCAT as a reference (ASCAT delivers data with high radiometric accuracy due to the averaging of multiple received pulses, see Section 2.1.4.1).

Figure 5.25 and Figure 5.26 show scatterplots with the backscatter coefficients plotted per time stamp for ASCAT and Sentinel-1 and ASCAT and ASAR WS. The green line represents the ASCAT backscatter data plotted against itself. The mean values of the different backscatter time series are represented by the horizontal and vertical lines. After the temporal matching of the datasets, the mean value of all Sentinel-1 and ASAR WS pixels within this ASCAT pixel was taken per time stamp. The averaging of the backscatter datasets was done in the linear domain and the results are expressed on a logarithmic scale. If the two regression lines for ASAR WS and Sentinel-1 would be congruent, then a one to one transfer of the ASAR WS parameters to Sentinel-1 would be feasible without any decline in SSM data quality. However, this was not the case in this study.

Figure 5.25 shows the backscatter analysis of an agricultural area (*location 3* from Sec-

tion 5.1.1). It can be seen that a bias is evident between Sentinel-1 and ASAR WS, resulting in values that are an average 2 dB lower than for Sentinel-1. Also, the wider range of backscatter values on the x-axis for ASAR WS corresponds to a higher sensitivity. Figure 5.26 shows the backscatter analysis of a densely vegetated area (*location 4* from Section 5.1.1. Here it seems that Sentinel-1 cannot detect a reasonable backscatter signal anyway, showing a more or less random distribution, which also reflects the weak correlation and RMSD performances in these areas.

The results of this backscatter analysis show that the usage of ASAR WS parameters in the Sentinel-1 algorithm is problematic. However, in order to realise the full potential of Sentinel-1 for soil moisture retrieval, one should revert to parameters calculated from Sentinel-1 data, which will soon be possible thanks to the incoming stream of Sentinel-1 data.

Figure 5.25: Analysis of Sentinel-1 and ASAR WS backscatter measurements at a soil moisture sensitive area. Sentinel-1 and WS backscatter averaged to 25 km and compared to ASCAT. The green line represents the ASCAT backscatter data plotted against itself.
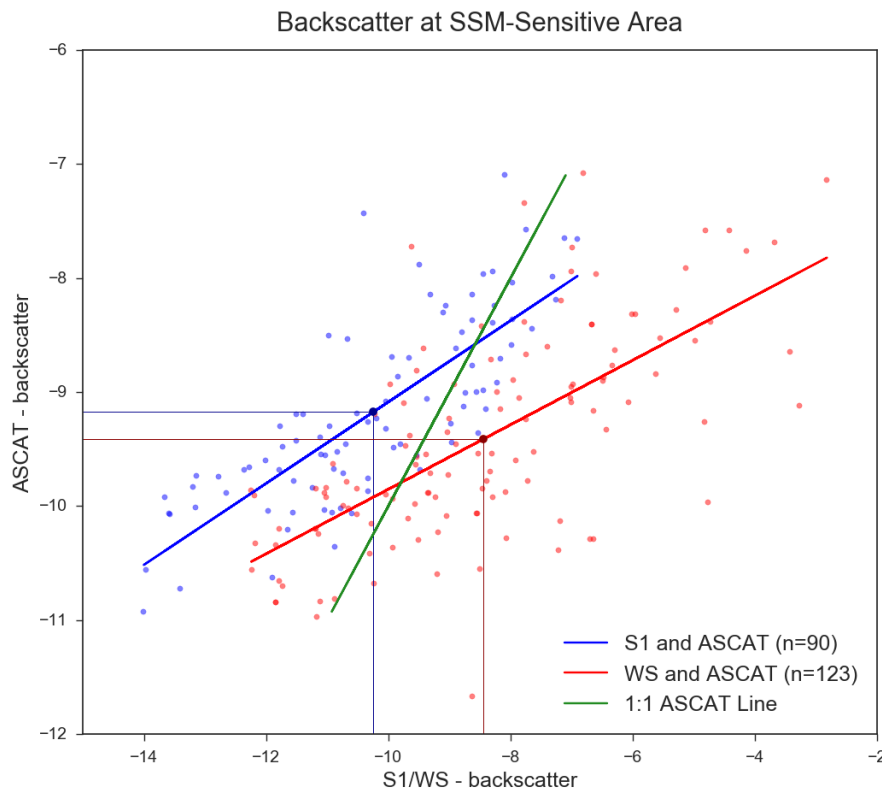
***Figure* 5.26:** *Analysis of Sentinel-1 and ASAR WS backscatter measurements at a densely ve-getated area. Sentinel-1 and WS backscatter averaged to 25 km and compared to ASCAT. The green line represents the ASCAT backscatter data plotted against itself.*
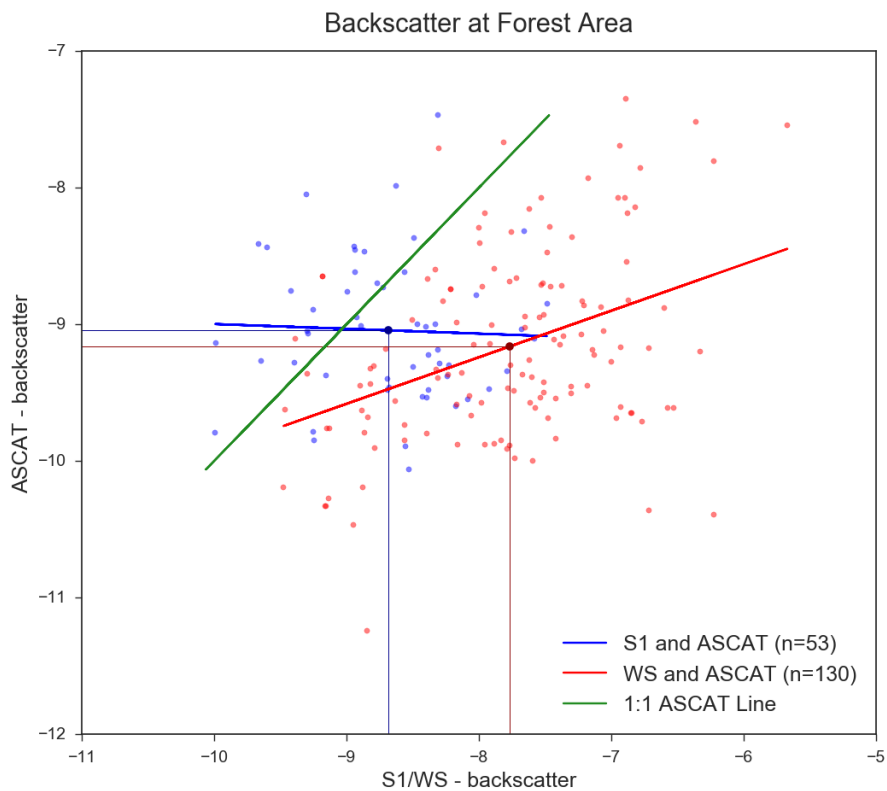
Chapter 6

Conclusion and Outlook

The knowledge of the spatial and temporal distribution of soil moisture is of great importance in several hydrological applications. These include, among others, hydrological models and weather forecasts, furthermore information about the soil moisture state provides important details for disaster management in flooding and drought situations.

The TU-Wien model is a method that uses active microwave measurements from satellites to retrieve information about the water content of the soil. There are already different soil moisture datasets available for scientific and operational use, providing resolutions of about 25-50 km (e.g. ASCAT, ERS). However, a much larger number of applications could be addressed if soil moisture data at a resolution of 1 km or finer becomes available [Wagner et al., 2009]. Such a high spatial resolution can only be achieved by synthetic aperture radars (SAR).

This study offered an insight into soil moisture retrieval from Envisat ASAR and Sentinel-1 backscatter data. The different acquisition strategies of ASAR result in inhomogeneous data archives which made it impossible for an operational use, in contrast the Sentinel-1 mission with its two satellites will soon be able to cover whole Europe every 1-3 days. Currently the Remote Sensing research group at TU-Wien retrieves soil moisture from Sentinel-1 data using TU-Wien model parameters that are calculated from ASAR Wide Swath data. In this study, an evaluation of the ASAR SSM datasets and the Sentinel-1 SSM datasets was performed in order to investigate if the transfer of the ASAR retrieval algorithm including the WS parameters to Sentinel-1 is feasible. Due to the lack of historical data (Sentinel-1A was launched in 2014) it is yet not possible to calculate reasonable parameters from Sentinel-1 data itself.

Due to the different observation periods of Envisat ASAR and Sentinel-1, it was not possible to compare their SSM products directly to each other. Hence, coarse resolution SSM data from ASCAT and GLDAS was used as reference datasets to perform the evaluation over a 600 km

x 600 km area in central Europe. The correlation coefficients as well as the root mean square differences were calculated between the SAR- and the reference-datasets.

A visual interpretation of the datasets showed that ASAR GM SSM has a higher noise level when compared to ASAR WS and Sentinel-1 which mostly results from lower radiometric resolution. This was also reflected in the time series analysis, featuring lower correlation coefficients for ASAR GM. The correlation and RMSD results show a better performance for ASAR WS than for Sentinel-1, which can be explained with the smaller sample size and shorter period of Sentinel-1 dataset. The overall pattern of the correlation and RMSD maps reflect the land cover structures in the study area. Therefore, the analysis was split up into several sub-classes using the Corine Land Cover map. Sentinel-1 did not yet reach the results from ASAR WS but already shows high correlation in areas without dense vegetation like grasslands or agricultural areas, whereas in densely vegetated areas Sentinel-1 SSM still seems to have problems.

Furthermore, the correlation layer was used to derive a mask that shows only pixels with a correlation coefficient higher than a certain threshold. Here, a high agreement of the masked and unmasked pixels to land cover was found and therefore locations can be detected where the SSM retrieval algorithm is capable to deliver valid results.

Additionally, backscatter comparisons between ASAR WS and Sentinel-1 for a soil moisture sensitive area and a densely vegetated area with ASCAT as a reference dataset showed a different behaviour of the backscatter measurements. This can be the result of a different calibration of the sensors and hence, the usage of ASAR WS parameters in the Sentinel-1 algorithm introduces errors and is not desirable.

Recently, the Remote Sensing Research Group at TU Wien performed first promising experiments using retrieval parameters solely calculated from Sentinel-1 data, which is important if one wants to realise the full potential of Sentinel-1 for soil moisture retrieval. In April 2016 also the second Sentinel-1 satellite was launched into space and both satellites together will provide data with almost daily coverage over Europe. This superior temporal coverage and radiometric accuracy, together with the high spatial resolution bear the great potential to capture spatio-temporal soil moisture patterns which were not observable from space before.

Appendix A

Additional Figures

A.1 Corine Land Cover Classification

Figure A.1 shows the different land cover types displayed in the Corine Land Cover map.

111 - Continuous urban fabric
112 - Discontinuous urban fabric
121 - Industrial or commercial units
122 - Road and rail networks and associated land
123 - Port areas
124 - Airports
131 - Mineral extraction sites
132 - Dump sites
133 - Construction sites
141 - Green urban areas
142 - Sport and leisure facilities
211 - Non-irrigated arable land
212 - Permanently irrigated land
213 - Rice fields
221 - Vineyards
222 - Fruit trees and berry plantations
223 - Olive groves
231 - Pastures
241 - Annual crops associated with permanent crops
242 - Complex cultivation patterns
243 - Land principally occupied by agriculture, with significant areas of natural vegetation
244 - Agro-forestry areas
311 - Broad-leaved forest
312 - Coniferous forest
313 - Mixed forest
321 - Natural grasslands
322 - Moors and heathland
323 - Sclerophyllous vegetation
324 - Transitional woodland-shrub
331 - Beaches, dunes, sands
332 - Bare rocks
333 - Sparsely vegetated areas
334 - Burnt areas
335 - Glaciers and perpetual snow
411 - Inland marshes
412 - Peat bogs
421 - Salt marshes
422 - Salines
423 - Intertidal flats
511 - Water courses
512 - Water bodies
521 - Coastal lagoons
522 - Estuaries
523 - Sea and ocean

Figure A.1: *Corine Land Cover Classification*

Table A.1 shows the different land cover type IDs from Figure A.1 that correspond to the various classes from Section 4.2.2.

	Land Cover Types ID
Agriculture	211, 212, 213, 221, 222, 223, 231, 241, 242, 243, 244, 321
Artificial	111, 112, 121, 122, 123, 124, 131, 132, 133, 141, 142
Forest	311, 312, 313, 323, 324, 333
Mountain	332, 334, 335
Water	322, 331, 411, 412, 421, 422, 423, 511, 512, 521, 522, 523

Table A.1: *Classification of different Land Cover Classes*

A.2 Additional Confusion Matrices

Figure A.2 and Figure A.3 show confusion matrices complementing Section 5.5.

(a) Rho=0.20

(b) Rho=0.30

(c) Rho=0.40

(d) Rho=0.50

(e) Rho=0.60

Figure A.2: *Confusion Matrices Sentinel-1*

(a) Rho=0.20

(b) Rho=0.30

(c) Rho=0.40

(d) Rho=0.50

(e) Rho=0.60

Figure A.3: *Confusion Matrices ASAR WS*

Bibliography

Barrett, B. and G. P. Petropoulos (2013). *Satellite remote sensing of surface soil moisture*. CRC Press: Boca Raton, FL, USA. 7

Bartalis, Z. (2009). Spaceborne scatterometers for change detection over land. 12

Bauer-Marschallinger, B., V. Naeimi, and W. Wagner (2015). Bodenfeuchtemessung durch radarsatelliten: Aktuelle entwicklungen zur erfassung auf lokaler ebene. *Österreichische Wasser-und Abfallwirtschaft 11*(67), 422–431. 6

Bauer-Marschallinger, B., D. Sabel, and W. Wagner (2014). Optimisation of global grids for high-resolution remote sensing data. *Computers & Geosciences 72*, 84–93. 20

Dostálová, A., M. Doubková, D. Sabel, B. Bauer-Marschallinger, and W. Wagner (2014). Seven years of advanced synthetic aperture radar (asar) global monitoring (gm) of surface soil moisture over africa. *Remote Sensing 6*(8), 7683–7707. 24, 40

Doubková, M., A. I. Van Dijk, D. Sabel, W. Wagner, and G. Blöschl (2012). Evaluation of the predicted error of the soil moisture retrieval from c-band sar by comparison against modelled soil moisture estimates over australia. *Remote sensing of environment 120*, 188–196. 40

Figa-Saldaña, J., J. J. Wilson, E. Attema, R. Gelsthorpe, M. Drinkwater, and A. Stoffelen (2002). The advanced scatterometer (ascat) on the meteorological operational (metop) platform: A follow on for european wind scatterometers. *Canadian Journal of Remote Sensing 28*(3), 404–412. 26

Gruber, A., W. Wagner, A. Hegyiova, F. Greifeneder, and S. Schlaffer (2013). Potential of sentinel-1 for high-resolution soil moisture monitoring. In *Geoscience and Remote Sensing Symposium (IGARSS), 2013 IEEE International*, pp. 4030–4033. IEEE. 3, 22

Hiebl, J., S. Reisenhofer, I. Auer, R. Böhm, and W. Schöner (2011). Multi-methodical realisation of austrian climate maps for 1971–2000. *Advances in Science and Research 6*(1), 19–26. 21

Hillel, D. (1998). *Environmental soil physics: Fundamentals, applications, and environmental considerations*. Academic press. 1

Hornacek, M., W. Wagner, D. Sabel, H.-L. Truong, P. Snoeij, T. Hahmann, E. Diedrich, and M. Doubková (2012). Potential for high resolution systematic global surface soil moisture retrieval via change detection using sentinel-1. *IEEE Journal of Selected Topics in Applied Earth Observations and Remote Sensing 5*(4), 1303–1311. 3

Kornelsen, K. C. and P. Coulibaly (2013). Advances in soil moisture retrieval from synthetic aperture radar and hydrological applications. *Journal of Hydrology 476*, 460–489. 9

Loew, A., R. Ludwig, and W. Mauser (2006). Derivation of surface soil moisture from envisat asar wide swath and image mode data in agricultural areas. *Geoscience and Remote Sensing, IEEE Transactions on 44*(4), 889–899. 3

Mudelsee, M. (2013). *Climate time series analysis*. Springer. 30

Naeimi, V., K. Scipal, Z. Bartalis, S. Hasenauer, and W. Wagner (2009). An improved soil moisture retrieval algorithm for ers and metop scatterometer observations. *Geoscience and Remote Sensing, IEEE Transactions on 47*(7), 1999–2013. 2, 14

Pathe, C., W. Wagner, D. Sabel, M. Doubkova, and J. B. Basara (2009). Using envisat asar global mode data for surface soil moisture retrieval over oklahoma, usa. *Geoscience and Remote Sensing, IEEE Transactions on 47*(2), 468–480. 3, 10, 14, 15, 18, 23, 25

Petropoulos, G. P., H. M. Griffiths, W. Dorigo, A. Xaver, and A. Gruber (2013). Surface soil moisture estimation: Significance, controls, and conventional measurement techniques. *Remote Sensing of Energy Fluxes and Soil Moisture Content*, 29–48. 2, 5

Rodell, M., P. Houser, U. e. a. Jambor, J. Gottschalck, K. Mitchell, C. Meng, K. Arsenault, B. Cosgrove, J. Radakovich, M. Bosilovich, et al. (2004). The global land data assimilation system. *Bulletin of the American Meteorological Society 85*(3), 381–394. 27

Schönwiese, C.-D. (2000). Praktische statistik für meteorologen und geowissenschaftler. *Zeitschrift für Geomorphologie 52*, 3. 29, 31

Scipal, K. (2002). *Global soil moisture retrieval from ERS scatterometer data*. na. 16

Seneviratne, S. I., T. Corti, E. L. Davin, M. Hirschi, E. B. Jaeger, I. Lehner, B. Orlowsky, and A. J. Teuling (2010). Investigating soil moisture–climate interactions in a changing climate: A review. *Earth-Science Reviews 99*(3), 125–161. 1, 5

Snoeij, P., M. Brown, M. Davidson, B. Rommen, N. Floury, D. Geudtner, and R. Torres (2011). Sentinel-1a and sentinel-1b csar status. In *SPIE Remote Sensing*, pp. 817902–817902. International Society for Optics and Photonics. 24

Torres, R., P. Snoeij, D. Geudtner, D. Bibby, M. Davidson, E. Attema, P. Potin, B. Rommen, N. Floury, M. Brown, et al. (2012). Gmes sentinel-1 mission. *Remote Sensing of Environment 120*, 9–24. 3, 24

Ulaby, F. T., D. G. Long, W. J. Blackwell, C. Elachi, A. K. Fung, C. Ruf, K. Sarabandi, H. A. Zebker, and J. Van Zyl (2014). Microwave radar and radiometric remote sensing. 7, 8

Ulaby, F. T., R. K. Moore, A. K. Fung, and A. House (1981). *Microwave remote sensing: active and passive*, Volume 1. Addison-Wesley Reading, MA. 6

Ulaby, F. T., R. K. Moore, A. K. Fung, and A. House (1982). *Microwave remote sensing: active and passive*, Volume 2. Addison-Wesley Reading, MA. 11

Von Storch, H. and F. W. Zwiers (2001). *Statistical analysis in climate research.* Cambridge university press. 30

Wagner, W. (1998). *Soil moisture retrieval from ERS scatterometer data.* Citeseer. 15, 17

Wagner, W., S. Hahn, R. Kidd, T. Melzer, Z. Bartalis, S. Hasenauer, J. Figa-Saldaña, P. de Rosnay, A. Jann, S. Schneider, et al. (2013). The ascat soil moisture product: A review of its specifications, validation results, and emerging applications. *Meteorologische Zeitschrift 22*(1), 5–33. 11

Wagner, W., G. Lemoine, and H. Rott (1999). A method for estimating soil moisture from ers scatterometer and soil data. *Remote Sensing of Environment 70*(2), 191–207. 2, 14, 17

Wagner, W., D. Sabel, M. Doubkova, A. Bartsch, and C. Pathe (2009). The potential of sentinel-1 for monitoring soil moisture with a high spatial resolution at global scale. In *Symposium of Earth Observation and Water Cycle Science*. 3, 60

Wagner, W., D. Sabel, M. Doubkova, M. Horná�ek, S. Schlaffer, and A. Bartsch (2012). Prospects of sentinel-1 for land applications. In *Geoscience and Remote Sensing Symposium (IGARSS), 2012 IEEE International*, pp. 1741–1744. IEEE. 22

Walker, J. P., G. R. Willgoose, and J. D. Kalma (2004). In situ measurement of soil moisture: a comparison of techniques. *Journal of Hydrology 293*(1), 85–99. 5

Woodhouse, I. H. (2005). *Introduction to microwave remote sensing*. CRC press. 7, 8, 10, 12, 13